

**Detector Integration of Severe Accident Management Instrumentation
for Robotic Applications at Nuclear Reactor Facilities**

by

Omar Nusrat

A thesis submitted to the
School of Graduate and Postdoctoral Studies in partial
fulfillment of the requirements for the degree of

Master of Applied Science

in

Nuclear Engineering

Faculty of Energy Systems and Nuclear Science

University of Ontario Institute of Technology (Ontario Tech University)

Oshawa, Ontario, Canada

August 2021

© Omar Nusrat, 2021

THESIS EXAMINATION INFORMATION

Submitted by: **Omar Nusrat**

Master of Applied Science in Nuclear Engineering

Detector Integration of Severe Accident Management Instrumentation for Robotic Applications at Nuclear Reactor Facilities

An oral defence of this thesis took place on August 13th, 2021 in front of the following examining committee:

Examining Committee:

Chair of Examining Committee	Dr. Jennifer McKellar
Research Supervisor	Dr. Edward Waller
Examining Committee Member	Dr. Scott Nokleby
Thesis Examiner	Dr. Rachid Machrafi

The above committee determined that the thesis is acceptable in form and content and that a satisfactory knowledge of the field covered by the thesis was demonstrated by the candidate during an oral examination. A signed copy of the Certificate of Approval is available from the School of Graduate and Postdoctoral Studies.

Abstract

In the aftermath of a nuclear accident, robots can be used to monitor and assess radiological contamination, preventing harmful exposure to plant personnel. In this work, several detectors were evaluated to be supplemented onto the Husky UGV. Specifically, the RadEye Gamma Survey Meter, the PurpleAir Air-Quality (PA) sensor, and the NaI(Tl) scintillator were examined and their measurement parameters optimized. Optimization was done to satisfy mitigation requirements outlined in regulatory severe accident management guidelines (SAMGs). A software component (Severe Accident Radioactivity Classification; SARC) was developed with the detector components, facilitating detector integration and analysis to aid emergency responders. For the RadEye, 20 seconds was determined to be the optimal collection time; the long term stability and short-term sensitivity of the PA was evaluated; and two spectra measured with the NaI(Tl) were examined. Future work involves further integration of SARC and the addition of advanced capabilities such as infrastructure damage detection.

Keywords: radiation detection; severe accident management; air sampling; robotics

Author's Declaration

I hereby declare that this thesis consists of original work of which I have authored. This is a true copy of the thesis, including any required final revisions, as accepted by my examiners.

I authorize the University of Ontario Institute of Technology (Ontario Tech University) to lend this thesis to other institutions or individuals for the purpose of scholarly research. I further authorize University of Ontario Institute of Technology (Ontario Tech University) to reproduce this thesis by photocopying or by other means, in total or in part, at the request of other institutions or individuals for the purpose of scholarly research. I understand that my thesis will be made electronically available to the public.

Omar Nusrat

Statement of Contributions

I hereby certify that I am the sole author of this thesis and that no part of this thesis has been published or submitted for publication. I have used standard referencing practices to acknowledge ideas, research techniques, or other materials that belong to others. Furthermore, I hereby certify that I am the sole source of the creative works and/or inventive knowledge described in this thesis.

Acknowledgements

First and foremost, I would like to thank my supervisor, Dr. Ed Waller. His thoughtful guidance, honest supervision, and unwavering support have allowed me to think, grow, and truly develop as a researcher. I have also learned more about health physics and nuclear engineering from his courses than from any book. I am extremely grateful to have learned firsthand from a world class expert like Dr. Waller, and I will always be grateful to him for taking me on as his student.

I would also like to thank my colleagues in the Health Physics and Environmental Safety Research group, as well as my colleagues in faculty at large; fellow graduate students, undergraduate students that I have had the pleasure of teaching, professors, and staff. I have learned something unique from every one of you, and I appreciate all of your support over these past two years. I will absolutely cherish our time together.

Lastly, to my family: for always inspiring, motivating, and supporting me, thank you. I love you very much.

The research performed in this thesis has been funded by the Natural Sciences and Engineering Research Council of Canada (NSERC) and the University Network of Excellence in Nuclear Engineering (UNENE).

Contents

Abstract.....	iii
Author’s Declaration.....	iv
Statement of Contributions	v
Acknowledgements.....	vi
List of Tables	ix
List of Figures	x
List of Abbreviations and Symbols.....	xiv
1. Introduction.....	1
1.1. Accident Prevention	1
1.2. Previous Nuclear Accidents	3
1.2.1. Chernobyl Accident.....	4
1.2.2. Fukushima Daiichi Accident	5
1.3. Radiological Effects of Severe Accidents	5
1.4. Severe Accident Management Guidelines	10
1.4.1. Canadian Regulatory Perspective	12
1.5. Radiation Measurement.....	13
1.5.1. Detectors	14
1.5.2. Spectroscopy.....	22
1.6. Use of Robotics in Nuclear Accidents	28
1.6.1. Radiation Mapping with Robotics	31
1.7. Purpose and Specific Aims	33
1.7.1. Specific Aims.....	33
2. Materials and Methods	34
2.1. Robotics Component.....	34
2.2. Characterizing Radiation Conditions	36
2.2.1. Collection Time Optimization	37
2.2.2. Isotope Identification	39
2.3. Air Sampling	41
2.3.1. PurpleAir Sensitivity Tests	44
2.3.2. Long Term Stability Tests	44

2.4.	Development of Software Component.....	45
2.4.1.	Response Algorithm	47
3.	Results	54
3.1.	Dose Rate Measurements	54
3.1.1.	Collection Time Optimization	54
3.2.	Isotope Identification.....	60
3.3.	Air Sampling	71
3.3.1.	PurpleAir Stability over Time.....	71
3.3.2.	Sensitivity Analysis	73
4.	Discussion.....	77
4.1.	Radiation Measurements	79
4.2.	Spectroscopy Results.....	81
4.3.	Air Sampling Measurements.....	81
4.4.	Comparison of UGVs and UAVs.....	84
4.5.	Practical Considerations	85
4.6.	Limitations	87
5.	Conclusions and Future Work	91
	References.....	93
	Appendix.....	109

List of Tables

No.	Title	Page
1	Typical values of LET, RBE, and W_R .	8
2	Tissue weighting factors from ICRP 103.	9
3	Summary of gas-filled detector characteristics.	18
4	Various type of photomultiplier devices compatible with scintillators.	20
5	Estimated radionuclide release in previous nuclear accidents.	24
6	Husky UGV specifications.	35
7	Features of the ThermoFisher RadEye.	37
8	Parameters from the NaI(Tl) spectra measurement. Spectra were obtained from Steinmeyer, P. from Radiation Safety Associates, Inc.	41
9	Features of the PurpleAir SD-II Sensor	43
10	SARC adaptation of ICRP 146 reference level limits by phase.	50
11	Mean and standard deviations for each collection time interval tested.	58
12	Comparison with natural background measurement in the Greater Toronto Area (GTA).	58
13	Identification of all peaks in the ^{60}Co , ^{57}Co , and ^{137}Cs spectra shown in Figures 35 to 39.	65
14	Spectroscopy parameters. Dead time could not be obtained as the spectra were obtained from Steinmeyer, P. from Radiation Safety Associates, Inc.	69
15	Battery life of Husky UGV with added on detectors. The Husky's battery lasts for 8 hours when on standby and 3 hours when moving. The total power available is 192V.	84
16	Total mass of additional components added to Husky UGV platform.	85
A.1	Radionuclides posing internal radiation hazards at CANDU facilities	109
A.2	Internal dose resulting from inhalation in hypothetical CANDU accident scenario for various CANDU release products	112

List of Figures

No.	Title	Page
1	The states of a nuclear power plant.	3
2	Map of the ^{137}Cs surface ground contamination released after the Chernobyl accident.	4
3	Increase in RBE as the incoming radiation LET increases.	7
4	Pathway of obtaining effective dose and equivalent dose based on a measured absorbed dose.	10
5	CNSC summary of plant states, defence in depth, and the relationship between emergency preparedness and accident management.	13
6	TLD crystals (shown on the left) and an OSL dosimeter shown on the right (figure from Kry et al., 2020).	15
7	Gas filled detectors operating at various voltage regions. Curve (a) corresponds to 1 MeV electrons and curve (b) corresponds to 100 keV electrons. Figure adapted from Knoll, 1989.	17
8	Various gas-filled radiation area meters are shown; (a) is an ionization chamber (the RO-20 manufactured by Thermo Fischer Scientific), (b) is a proportional counter, and (c) is a Geiger-Müller counter.	18
9	Typical photomultiplier tube shown. The glass casing and entrance window (on the right side) are clearly visible.	21
10	Schematic diagram of a typical photomultiplier tube and its components.	21
11	Photomultiplier tube operation principles.	22
12	Decay scheme for ^{137}Cs into ^{137}Ba via beta decay.	25
13	Decay scheme of ^{60}Co .	26
14	Photon interaction likelihood as a function of energy and the absorber's atomic number.	27
15	Ground based robotic systems from both past and present that have been used in nuclear settings. (A) is the 'Surveyor bot', (B) Pioneer 1 used for imaging inside of the Chernobyl sarcophagus, (C) JAEA Robot for gamma ray imaging, (D) NUSTEC MoniROBO-A and B used for	30

infrastructure damage detection, (E) the VaultBot developed by researchers at the University of Texas Austin, and (F) the Spot robot developed by Boston Dynamics currently used at Ontario Power Generation (OPG).

- 16 Husky UGV at the Ontario Tech University campus (left) and its 35
schematic designs on the right.
- 17 ThermoFisher RadEye G Gamma Survey Meter. The image on the right 36
shows the BLE adaptor at the back of the RadEye.
- 18 The handheld RadEye G experimental setup for 20 second dose rate 39
collection time, 1 meter over the surface of the ground.
- 19 Universal Spectrum Analyzer (URSA)-II device which couples to the 40
NaI(Tl) scintillator. Both the side view (left) and connections (right) are
shown.
- 20 The measuring component of the setup. This casing contains the NaI(Tl) 40
scintillator coupled to a photomultiplier tube using optical glue.
- 21 PurpleAir SD-II Air Quality Detector. On the left, the side view of the 42
detector is shown while on the right, the two lasers used to measure air
quality are shown.
- 22 Experimental setup of PurpleAir SD-II sensor. On the left, the device ID 45
and barcode are redacted for privacy. On the right, the brightness of the
image was increased to increase the visibility of the underside of the PA.
- 23 General workflow of SARC software. 48
- 24 Main' tab of SARC software. Features include a quick estimate of air 49
quality based on number of particles present and a quick estimate of
effective dose based on dose rate of a selected radioisotope.
- 25 'Gamma Dose Rate' tab of SARC software. 51
- 26 'Air Sampling' tab in SARC. Data collected by the PurpleAir sensor can 52
be loaded and visualized here.
- 27 Isotope ID' tab in SARC 53
- 28 Dose rate measured using 1 s collection time on the RadEye detector. 54
- 29 Dose rate measured using 5 s collection time on the RadEye detector. 55

30	Dose rate measured using 20 s collection time on the RadEye detector.	55
31	Dose rate measured using 40 s collection time on the RadEye detector.	56
32	Dose rate measured using 60 s collection time on the RadEye detector.	56
33	Dose rate measured using 120 s collection time on the RadEye detector.	57
34	Channel-to-energy calibration for the ^{137}Cs used in the URSA analysis software.	60
35	Energy spectra for ^{137}Cs measured using the URSA NaI(Tl) detector and analyzed using the URSA software. Data provided by Steinmeyer, P. from Radiation Safety Associates, Inc. Peak labels correspond to Table 12.	61
36	Energy spectra for ^{137}Cs measured using the URSA NaI(Tl) detector and analyzed using the URSA software shown with the y-axis in the logarithmic scale. Data provided by Steinmeyer, P. from Radiation Safety Associates, Inc.	62
37	Channel-to-energy calibration for the mixed field data used in the URSA analysis software.	63
38	Energy spectra for the mixed field measured using the URSA NaI(Tl) detector and analyzed using the URSA software. Data provided by Steinmeyer, P. from Radiation Safety Associates, Inc.	64
39	Energy spectra for the mixed field measured using the URSA NaI(Tl) detector and analyzed using the URSA software shown with the y-axis in the logarithmic scale. Data provided by Steinmeyer, P. from Radiation Safety Associates, Inc.	65
40	Stability of PurpleAir measurement over the course of two months (March 4 th 2021 to May 1 st 2021) with a 6 hour averaging time.	70
41	Air sampler data collected using the PurpleAir device after talcum powder exposure for several particulate sizes including: 0.3, 0.5, 1.0, 2.5, 5.0, and 10.0 μm .	71
42	Air sampler data collected using the PurpleAir device after talcum powder exposure for particles of size 1.0 and 5.0 μm sampled per dl.	72

43	Air sampler data collected using the PurpleAir device after dust exposure for several particulate sizes including: 0.3, 0.5, 1.0, 2.5, 5.0, and 10.0 μm particles per dl.	73
44	Air sampler data collected using the PurpleAir device after dust exposure for several particulate sizes including: 1.0 and 5.0 μm .	74
45	Summary of data to dosimetry process with the instrumentation used.	82
46	Malfunctioning internal computer of Husky UGV	86
47	Close-up of the GRIMM Portable Aerosol Spectrometer	87
A.1	Satellite view of Pickering Nuclear Generating Station	110

List of Abbreviations and Symbols

Abbreviations in the table below are listed in order of appearance in this document.

AMCL	Adaptive Monte Carlo Localization
AOO	Anticipated Operational Occurrence
APD	Avalanche Photodiode
ARS	Acute Radiation Syndrome
BDBA	Beyond Design Basis Accident
CANDU	Canada Deuterium Uranium
CNSC	Canadian Nuclear Safety Commission
COVID-19	Coronavirus Disease 2019
CZT	Cadmium Zinc Telluride
DBA	Design Basis Accident
DCF	Dose Conversion Factor
DRZ	Dangerous Radiation Zone
EOP	Emergency Operating Procedures
GTA	Greater Toronto Area
GUI	Graphical User Interface
IAEA	International Atomic Energy Agency
IAMP	Integrated Accident Management Program
ICRP	International Commission on Radiological Protection
IFB	Irradiated Fuel Bay
IMBA	Integrated Modules for Bioassay Analysis
INES	International Nuclear and Radiological Event Scale
IoT	Internet of Things
JAEA	Japan Atomic Energy Agency
LET	Linear Energy Transfer
LiDAR	Light Detection and Ranging
LOCA	Loss of Cooling Accident
MCA	Multi-Channel Analyzer

NCRP	National Council on Radiation Protection and Measurements
NIST	National Institute of Standards and Technology
PMT	Photomultiplier Tube
PRD	Personal Radiation Detector
RBE	Relative Biological Effectiveness
RBMK	High-Powered Channel Type (translated from Russian)
ROS	Robot Operating System
SAMG	Severe Accident Management Guidelines
SARC	Severe Accident Radioactivity Classification
SLAM	Simultaneous Localization and Mapping
TEPCO	Tokyo Electric Power Company
TLD	Thermoluminescent Dosimeter
UAV	Unmanned Aerial Vehicle
UGV	Unmanned Ground Vehicle
URSA	Universal Radiation Spectrum Analyzer
USSR	Union of Soviet Socialist Republics

1. Introduction

According to the World Nuclear Association, there have only been two major nuclear accidents in history despite the operation of over 18,000 nuclear reactor-years spanning the past 60 years.⁴ In comparison, since 2012, the aviation industry has suffered from 1,139 accidents with varying levels of severity. Despite seeming large, this number has greatly decreased compared to previous decades.⁵ This statistic is a testament to the nuclear industry's excellence in safety standards and design. A severe accident in the nuclear context can have devastating consequences. The radiological, social, political, and economic consequences would be immense and the lives of the individuals living close to the accident site would be either harmed or forever changed.^{6,7}

1.1. Accident Prevention

Since there have only been a small number of nuclear accidents throughout history, nuclear safety specialists have utilized a 'defence in depth' approach to preventing future incidents from occurring. Defence in depth is a layered approach that ensures safe nuclear plant operation in the occurrence of an adverse event that has a low probability of occurring, but a high severity if it does.⁸ Key components of the defence in depth strategy include the prevention, control, and mitigation of different possible event states within nuclear power plants.⁹

The first potential state is 'normal plant operations', followed by 'anticipated operational occurrences' or AOOs.¹⁰ Anticipated operational occurrences are events that

are anticipated to occur during the lifetime of the plant, however they are classified as out of normal operations. Examples of anticipated operational occurrences include the inadvertent withdrawal of a single control rod or the inadvertent opening of steam relief valves. During anticipated operational occurrences, the nuclear plant will continue to remain in operation as its safety systems are designed to handle these events. The third type of event is the design basis accident, or DBA. These are accidents for which there is a specific defence in the nuclear facility as per regulatory requirements. As an example, if there is a loss of cooling accident (LOCA) in the irradiated fuel bay (IFB), there are design features built into the system to minimize the accident's impact. In this example, there are emergency pump systems which have been installed to ensure that the fuel remains cool.

The final type of event is the 'beyond design basis accident' or BDBA. These accidents are entirely unpredictable and can result from natural disasters or circumstances that are outside of the design basis of the plant safety features. Severe accidents are typically classified as BDBAs.¹¹ The probability of these events occurring is visualized in Figure 1. The guidelines on how severe accidents are managed will be discussed in Section 1.4.

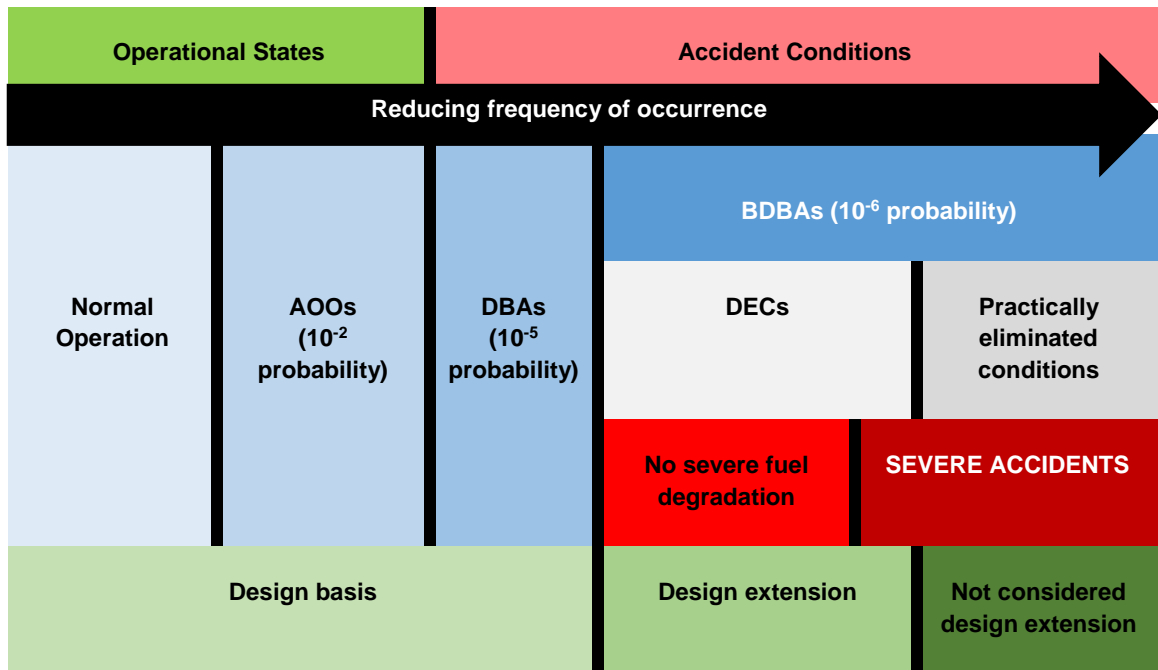


Figure 1: The states of a nuclear power plant; adapted from the Canadian Nuclear Safety Commission (CNSC) Regulatory Document 2.4.1.⁹ In this figure, the plant states described are shown. Going from left to right, the likelihood of an event occurring in the plant decreases, however, the severity if it does occur increases.

1.2. Previous Nuclear Accidents

Despite their small number of occurrences, the impact of past severe nuclear accidents has been vast. The International Atomic Energy Agency (IAEA) classifies accidents based on their severity using the International Nuclear and Radiological Event Scale (INES).¹² This scale is based upon the societal and environmental impact and ranks accidents on a scale of 0 to 7, with 7 being the most severe. There have only ever been two events which

were ranked as 7 by the IAEA: 1) the Chernobyl incident, and 2) the Fukushima-Daiichi incident.

1.2.1. Chernobyl Accident

The Chernobyl accident occurred on April 26th, 1986, near Pripyat, a now abandoned town near the city of Chernobyl, located in the north of modern-day Ukraine. Formerly, this city fell under the jurisdiction of the Union of Soviet Socialist Republics (USSR). Widely accepted as the most severe nuclear accident in history, it has been pictorialized in several films and documentaries.^{13,14} This accident occurred on Unit 4 of the Lenin Nuclear Power Plant. In the high-powered channel type (RBMK) reactor, the power rapidly increased during a main pump trip test. Unfortunately, this process could not be terminated, leading to a steam explosion in the reactor.^{15,16}

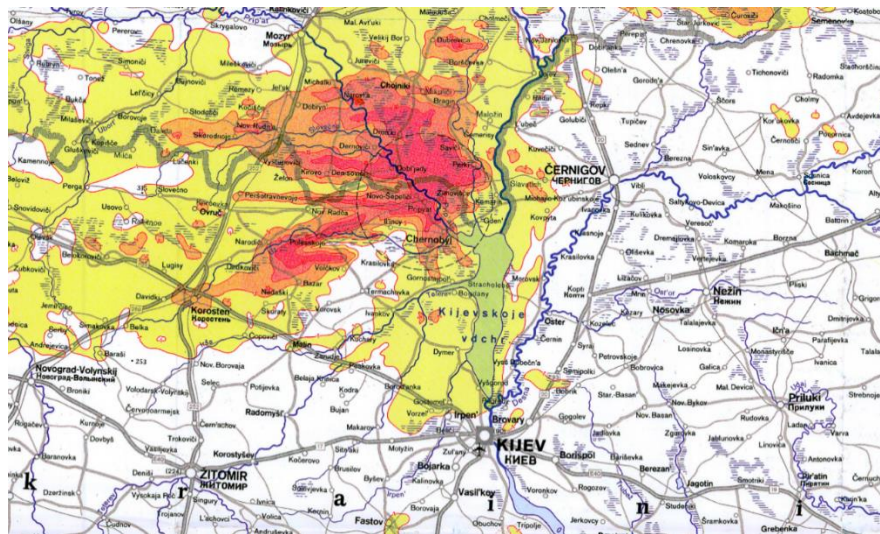


Figure 2: Map of the ¹³⁷Cs surface ground contamination released after the Chernobyl accident.¹⁷

1.2.2. Fukushima Daiichi Accident

The second major nuclear accident that has occurred is the Fukushima accident. Also classified as a level 7 accident under the INES scale, the accident at the Fukushima-Daiichi nuclear power plant is considered to be the second most devastating nuclear disaster in history. The disaster occurred on March 11th, 2011; an earthquake with a magnitude of 9.0 on the Richter scale occurred off of the east coast of Japan resulting in a large tsunami. One of the tsunami's most affected areas was the Fukushima prefecture. In this prefecture, there were two nuclear plants operated by the Tokyo Electric Power Company (TEPCO) – Fukushima-Daiichi and Fukushima-Daini. The tsunami struck the coast with a height of 14 metres, clearing the walls surrounding the plant and resulting in meltdowns of three reactors, solely at the Fukushima-Daiichi site.¹⁸

It was later determined that TEPCO did not integrate the necessary safety features into the Fukushima-Daiichi facility safety framework to effectively manage the accident. Specifically, they did not have design features to prepare for natural disasters or public evacuation events. In contrast, the sister nuclear plant, Fukushima-Daini, did have the correct measures in place and the appropriate accident management plans caused the reactors to shut down as a result of the impending tsunami.^{2,19,20}

1.3. Radiological Effects of Severe Accidents

The International Commission on Radiological Protection (ICRP) defines a large nuclear accident as one in which a significant amount of radioactive material is released into the environment.²¹ Radiation received by individuals in an accident setting is

quantified through the concept of effective dose. Effective dose is essentially the absorbed dose adjusted for the radiation quality and tissue type. This formalism will be briefly described below.

Absorbed dose is defined as the energy absorbed per unit mass in tissue. This is a purely physical quantity and is dependent upon the energy absorbed from the incoming radiation as well as the density of the absorbing material. Absorbed dose is reported in units of Gray (Gy), given that 1 Gy is equal to 1 Joule of energy absorbed per kilogram of absorber material. Mathematically, absorbed dose can be written as,

$$D_{Absorbed} = \frac{dE_{Absorbed}}{dm}, [Gy]. \quad (1)$$

While absorbed dose and biological effect do correlate, the amount of damage to tissue is highly dependent upon radiation quality. Radiation quality is also referred to as the linear energy transfer, or LET. LET is simply the ionization density of the incident radiation along its path. Higher LET radiation will deposit energy closer together and thus is more likely to cause cell death. Various types of radiation have distinct LET; for example, photons from ^{60}Co have an LET of less than 0.5 keV/ μm while 10 MeV protons can have LET values of up to 5.0.^{22,23}

The increase in cell death due to LET is captured through the concept of relative biological effectiveness, or RBE. RBE is defined as the ratio of doses from two different radiation types to achieve the same biological endpoint (Figure 3).^{24,25}

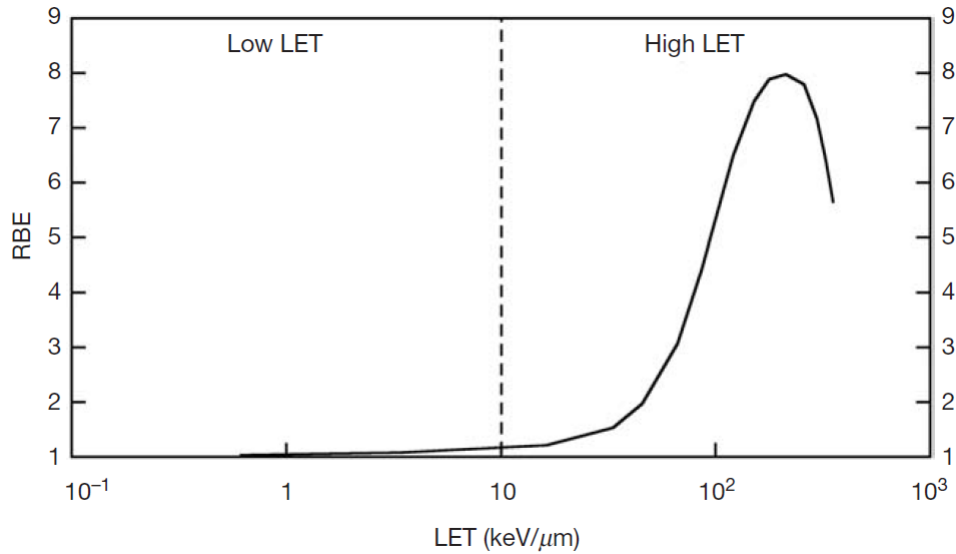


Figure 3: Increase in RBE as the incoming radiation LET increases.²⁶

The concept of RBE is mainly used in the medical radiation context. For radiation safety and nuclear accident response, the quantity used would be the ‘radiation weighting factor’, or W_R . This concept was initially introduced in 1990 by the ICRP and then updated in 2003 through ICRP Publication 92.²⁷ W_R is a quantity which encompasses the RBE ranges for each particle type and is a multiplication factor used to convert absorbed dose to equivalent dose (H_T), which is given in units of Sieverts (Sv). Typical values of W_R are shown in Table 1.

Table 1: Typical values of LET, RBE, and W_R .^{23,27,28}

Radiation Type	LET (keV/μm)	RBE	W_R
^{60}Co γ-rays	0.2	1.0	1
250 kV x-rays	2.0	1.1	1
10 MeV protons	4.7	5	2
2.5 MeV α-particles	166	20	20

In order to obtain the effective dose (E) from equivalent dose, the tissue weighting factor (W_T) must be used. This weighting factor accounts for the different radiosensitivity of various tissues. These weighting factors were also introduced by the ICRP and the latest version can be found in ICRP Publication 103.²⁹ The entire process of converting absorbed dose to equivalent dose and then effective dose can be found in Figure 4. It is also important to note the relationship of these dose quantities and their radiobiological effects, namely deterministic and stochastic effects. For a particular effect to manifest, a minimum threshold dose must be exceeded. Below the threshold, there is no effect. This is known as a deterministic effect, which also typically increases in severity as a function of dose. Examples of deterministic effects include skin reddening and acute radiation syndrome (ARS). On the other hand, stochastic effects are effects that may or may not occur. While the severity of stochastic effects does not change as a function of dose, their likelihood does. As dose increases, the probability of stochastic effects occurring increases. It is also important to note that there is no threshold for stochastic effects. An example of a stochastic effect is the development of cancer.²⁹

Table 2: Tissue weighting factors from ICRP 103.²⁹

Tissue	W_T
Testes	0.08 (0 for female)
Ovaries	0.08 (0 for male)
Bone surface	0.01
Bladder	0.04
Bone marrow	0.12
Brain	0.01
Breast	0.12
Colon	0.12
Liver	0.04
Lungs	0.12
Esophagus	0.04
Salivary glands	0.01
Skin	0.01
Stomach	0.12
Thyroid	0.04

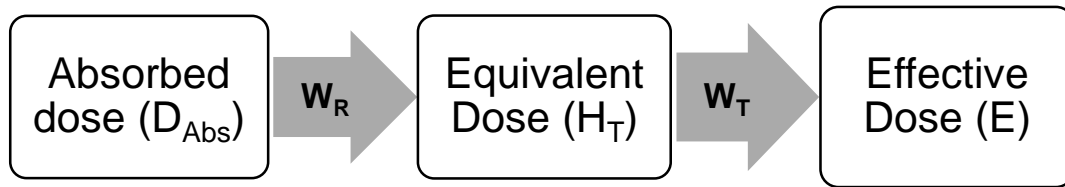


Figure 4: Pathway of obtaining effective dose and equivalent dose based on a measured absorbed dose. W_R and W_T are the radiation and tissue weighting factors, respectively.^{27,29}

1.4. Severe Accident Management Guidelines

As discussed earlier, the stages of the ‘defence in depth’ strategy in nuclear power plants can be classified based on both the severity and likelihood of occurrence.⁹ As the likelihood of occurrence increases, the frequency of the event happening also proportionally increases, and vice versa. To this end, certain procedures are developed within the plant safety protocols to address the approach necessary in the event that a low frequency incident occurs. In the rare occurrence of a BDBA (beyond design basis accident), severe accident management protocols are activated. The International Atomic Energy Agency (IAEA) defines ‘accident management’ as a three-step process in which actions are taken as the situation evolves to prevent its escalation, mitigate its consequences, and achieve a long-term, safe stable state.

The main IAEA guidance document regarding accident management directs national regulators on how to develop, establish, and implement accident management programs into their regulations and thus individual plant operating procedures. This allows

for the effective application of the defence in depth measures for various nuclear plant states.³⁰ The developed program would also encompass all necessary emergency procedures and equipment that is required to halt the progression of the accident and mitigate its effects.

Severe accident management guidelines (SAMGs) are one of the two types of accident management guidance procedures followed to restore safety in the event of an accident occurring at a nuclear power plant. The other type of management guidance procedures is the ‘emergency operating procedures’, or EOPs. The former is in reference to preventing the degradation of fuel rods or by delaying the time when degradation occurs to preserve the safety functions of the plant.³¹ These emergency procedures are implemented before SAMGs are enacted.

As previously mentioned, SAMGs are meant to mitigate significant degradation of the fuel rods when a severe accident has occurred. There are three main components in the SAMG:

- 1) Maintenance of integrity of barriers to fission products (such as containment).
- 2) Limiting (or completely avoiding) any fission product releases into the environment.
- 3) Returning to a long-term stable state.

In the CANDU reactor context, the first point about maintaining barrier integrity also includes maintaining the integrity of the pressure and calandria tubes. While much of the accident management regulations focus on the actions that operators must take in

mitigating accident conditions, there is a specific section regarding the environment in and around the nuclear plant. These sections focus on monitoring environmental conditions, maintenance of robust hardware, and use of the correct equipment.

The IAEA severe accident management guideline document³² states that,

‘To ensure that the likelihood of occurrence of an accident with radiological consequences is extremely low and that the radiological consequences of such an accident would be mitigated to the fullest extent practicable.’

In order to fulfill this mandate, several measures must be taken. These include the active monitoring of the nuclear environment during and after an incident occurs. As technology has advanced in the past few decades, this can be done using robotic and autonomous platforms. This was a visible component of the monitoring response in the Fukushima-Daiichi incident.³³ In a nuclear accident scenario, monitoring would not be restricted to only nuclear operators in the plant.

1.4.1. Canadian Regulatory Perspective

The CNSC’s approach to addressing the IAEA’s regulatory requirements is to outline Integrated Accident Management Program (IAMP) requirements for nuclear facilities and their respective licensees. The CNSC defines their severe accident management program as one that establishes: 1) the immediate steps that must be taken to minimize damage to the reactor core both in the short and long term, 2) the preparatory precursors to be able to carry out the first point, and 3) management of CANDU fission products.

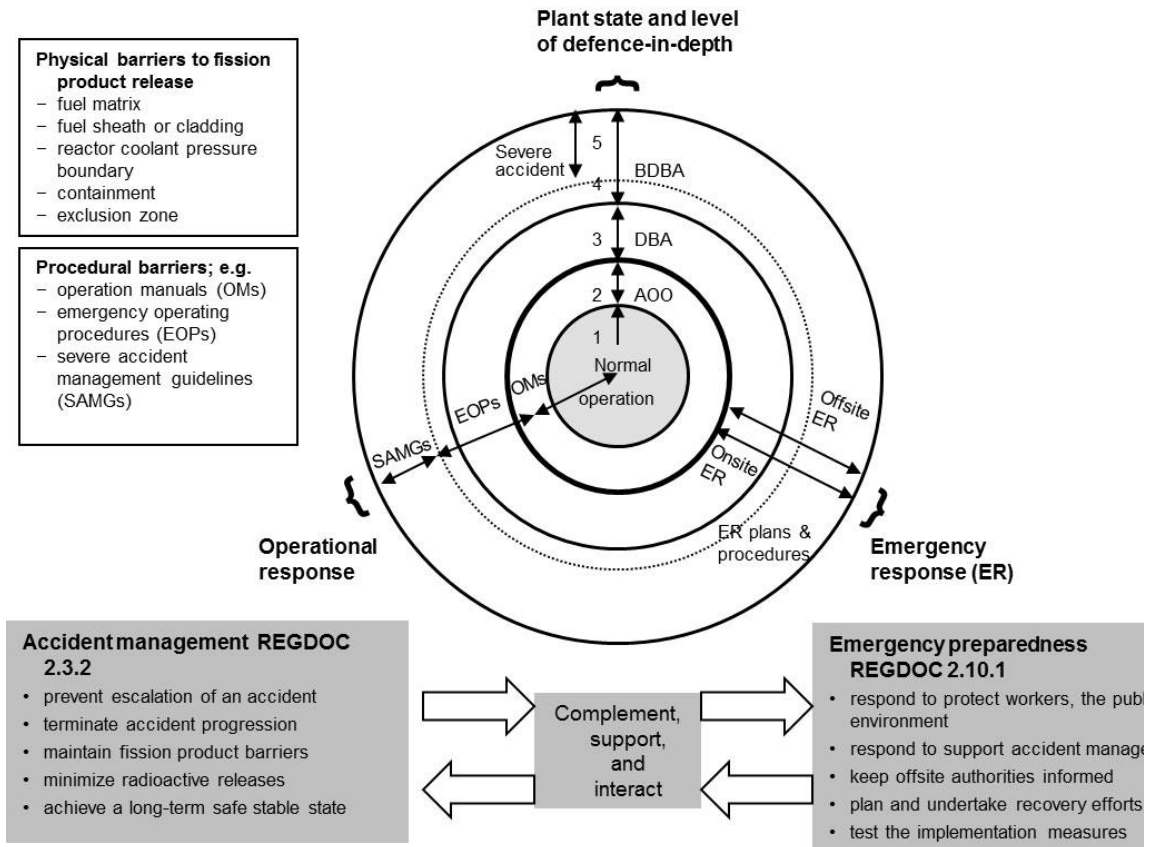


Figure 5: CNSC summary of plant states, defence in depth, and the relationship between emergency preparedness and accident management.³⁴

1.5. Radiation Measurement

In this work, a novel approach to nuclear accident response using modified unmanned ground vehicles (UGVs) is proposed. In this framework, UGVs would be equipped with a set of specialized detection equipment that would allow accident responders to remotely determine: 1) the amount of radiation (radiation dose), 2) the type of radioisotopes, and 3) the particulate size and magnitude of dispersion. The radiation dose and the type of radioisotope are determined using the outputs of an energy compensated Geiger-Müller counter and a NaI(Tl) scintillator for spectroscopy. The particulate size and dispersion

magnitude are determined using an air sampling device capable of particle size discrimination. The general principles upon which these detectors are based will be described in this section.

1.5.1. Detectors

In this work, the optimal radiation measurement tools for the post-accident scenario must be determined. There are several types of radiation detectors that can be considered. In this section, the different types of radiation detectors and their underlying principles will be described.

We will consider two main categories of detectors: personal dosimeters and radiation monitors. Personal dosimeters are carried by nuclear energy workers in environments such as nuclear power plants and radiotherapy cancer hospitals. According to guidelines and as seen in previous incidents, in an accident scenario, workers within or near the site would be equipped with a personal dosimeter.^{7,35-37} Personal dosimeters typically measure the dose equivalent in soft tissue passively over time and must be processed to obtain their readings. Two commonly used personal dosimeters are thermoluminescent dosimeters, commonly referred to as TLDs, and optically stimulated luminescent dosimeters (OSLDs), shown in Figure 6. Thermoluminescent dosimeters are typically composed of Lithium Fluoride doped with either Magnesium (LiF:Mg) or Titanium (LiF:Ti). When irradiated, electrons are excited from the valence band to the conduction band and become 'trapped' post-excitation. In order to read the integrated dose measured by the TLD, these materials can be heated to high temperatures (up to 400° C), allowing for the electron to complete its transition and a photon to be released.^{38,39} These photons are then quantified, and dose is measured. Conversely, OSLDs operate in a similar

manner, however, the annealing process (which allows electrons to leave the trap) is done through optical stimulation (light) instead of heating. OSLDs are composed of Carbon-doped Aluminum Oxide ($\text{Al}_2\text{O}_3:\text{C}$) and have become increasingly common in recent years due to their ease of use compared to TLDs.^{40,41}



Figure 6: TLD crystals (shown on the left) and an OSL dosimeter shown on the right (figure from Kry et al., 2020).³⁹

As mentioned previously, in order to measure the amount of radiation dose in a given area, area radiation monitors or survey meters must be used. Area monitors are fixed in space, and passively measure changes in dose, while survey meters are used to survey external radiation fields. These detectors are typically much larger than the passive personal dosimeters described above. Survey meters can be classified into two types: solid state detectors or gas filled detectors.²⁶

Generally, gas filled detectors work based upon the principle that gas contained in a cavity can be ionized by incoming radiation. If a sufficient voltage is applied between the boundaries of the cavity, the radiation-induced ions will accelerate toward the oppositely charged electrode. If a very high voltage is applied, the ion will cause further ionization on its way to the electrode, magnifying the signal generated by the initial incoming radiation.

This magnification is referred to as the ionization cascade. This cascade is also referred to as the Townsend avalanche in literature.^{42,43}

Different types of gas filled detectors will operate at various applied voltages (Figure 7). These gas-filled detectors include ionization chambers, proportion counters, and Geiger-Müller counters. Ionization chambers have large volumes containing gas and operate within the ionization chamber region. At these relatively low voltages, the amplification cascade does not contribute a significant amount to the overall signal, thus leading to a more precise measurement. Operating voltages for ionization chambers usually range from 150 to 400 V.⁴⁴ Proportional counters operate at higher voltages and thus exhibit the multiplication cascade described previously. Proportional counters are most suited for measurements in low radiation environments because at larger dose rates, the proportional counter suffers from large amounts of noise and dead times. Dead time is defined as the time interval (after an event) in which the detector cannot measure a subsequent count.⁴⁵ Finally, the third type of gas-filled detector is the Geiger-Müller counter. In this detector, the avalanche cascade occurs with an even greater magnitude and is operated at a voltage past which the detector would continuously discharge. Due to this, the detector is suited to measuring very low amounts of radiation. It is important to note that the volume containing the gas is typically a cylindrical volume with the outer wall as one electrode and the second electrode in the centre of the cavity. These detectors are typically shaped as cylinders because the cylindrical geometry allows for uniform gas multiplication. Several detector characteristics are summarized in Table 3 and examples of all three detectors are shown in Figure 8.

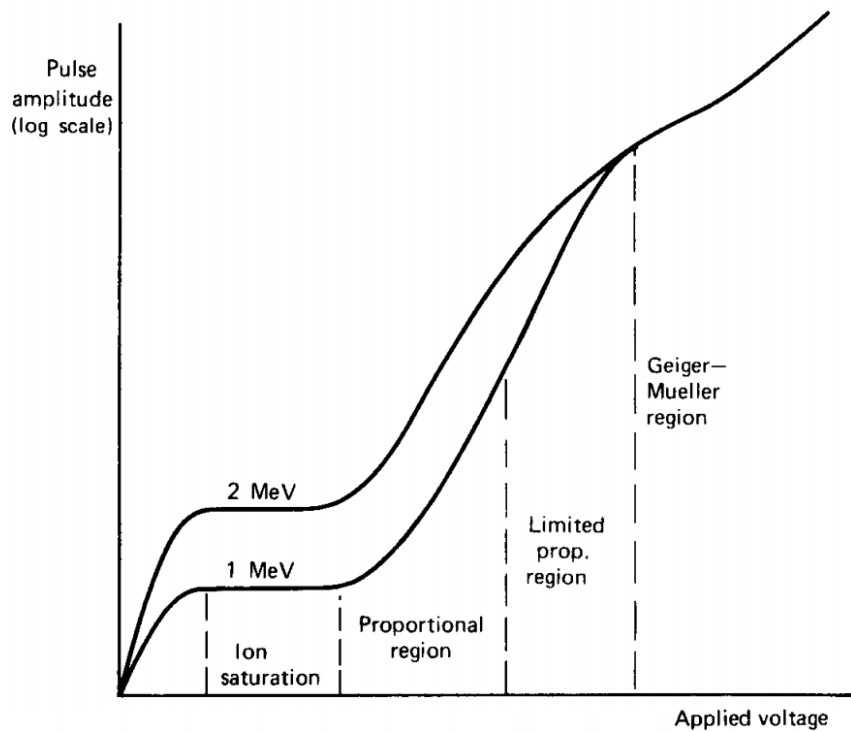


Figure 7: Gas filled detectors operating at various voltage regions. Curve (a) corresponds to 1 MeV electrons and curve (b) corresponds to 100 keV electrons.

Figure adapted from Knoll, 1989.⁴⁶



Figure 8: Various gas-filled radiation area meters are shown; (a) is an ionization chamber (the RO-20 manufactured by Thermo Fischer Scientific⁴⁷), (b) is a proportional counter⁴⁸, and (c) is a Geiger-Müller counter⁴⁹.

Table 3: Summary of gas-filled detector characteristics.

Gas-Filled Detector	Operating Voltage ⁴⁶	Advantages ⁴⁶	Disadvantages ⁴⁶	Commercial Products
Ionization Chamber	150 V – 400 V	<ul style="list-style-type: none"> • Lowest dead time • Accurate measurements 	<ul style="list-style-type: none"> • Large signal required for detection 	Thermo-Fischer Scientific RO-20
Proportional Counter	800 V – 1,600 V	<ul style="list-style-type: none"> • Energy information is preserved, allowing for spectroscopy 	<ul style="list-style-type: none"> • Moderate dead time 	Canon E6895B
Geiger-Müller Counter	500 V – 2,000 V	<ul style="list-style-type: none"> • Very large amplification of signal (by a factor of 10^9-10^{10}) 	<ul style="list-style-type: none"> • Large dead time • Lack of energy information 	Ludlum – Model 26-1 Frisker

Detectors that are based on solid state principles, not gas-filled multiplication, also exist. These include scintillators and semiconductor diodes. Scintillators are materials which emit light when they interact with radiation. This class of detector can be divided into two parts: organic (plastic) and inorganic (crystals). Organic scintillators consist of benzene ring-based molecules which excite upon interacting with radiation, and then de-excite, releasing a visible photon.^{50,51} Inorganic scintillators are crystal lattice structures in which electrons can get trapped in between the conduction and valence bands due to impurities in the lattice. The impurities in these inorganic scintillators is caused through doping.⁵²⁻⁵⁴ This is the reason behind common scintillators such as NaI or CsI are usually doped with a high Z element such as Thallium.^{55,56} Inorganic scintillators such as NaI(Tl) can also be used for the purposes of resolving the energy spectra of incoming radiation, which facilitates isotope identification. This will be further discussed in the following section.

In both organic and inorganic scintillators, the light produced through radiation interactions is quantified through the use of a photomultiplier device. These devices convert visible photons into a measurable electrical signal. There are several types of photomultipliers; these include photomultiplier tubes (PMTs), photodiodes, and avalanche photodiodes (APDs). Photomultiplier tubes are the most commonly used type of device since it is capable of the largest magnification of signal (up to 10^{10}). Table 4 compares these different photomultiplier devices.

Table 4: Various type of photomultiplier devices compatible with scintillators.⁵⁷

Type	Amplification	Main Use	Commercial Products
Photomultiplier tube (PMT)	$10^7 - 10^{10}$	<ul style="list-style-type: none"> • Radiation Spectroscopy • Low level radiation detection 	Hamamatsu R329
Photodiode	1-10	<ul style="list-style-type: none"> • Low voltage required • Used in high activity environments 	Hamamatsu S8745
Avalanche photodiode	60	<ul style="list-style-type: none"> • PET Imaging 	Hamamatsu S2384

Photomultiplier tubes are generally cylindrical in shape, have glass walls surrounded by metal casing, and also have a small entrance window (Figure 9 and 10). Incoming photons interact with the entrance window, releasing several electrons into the PMT's vacuum tube. Once in the vacuum tube, the electrons are drawn to successive electrodes (called dynodes). Each dynode has a greater potential difference than the previous one, causing increasing numbers of electrons to be produced. This process repeats several times (most PMTs have approximately 7-10 dynodes), greatly amplifying the initial signal.⁵⁸ The general principles of their operation is shown in Figure 11.



Figure 9: Typical photomultiplier tube shown.⁵⁹ The glass casing and entrance window (on the right side) are clearly visible.

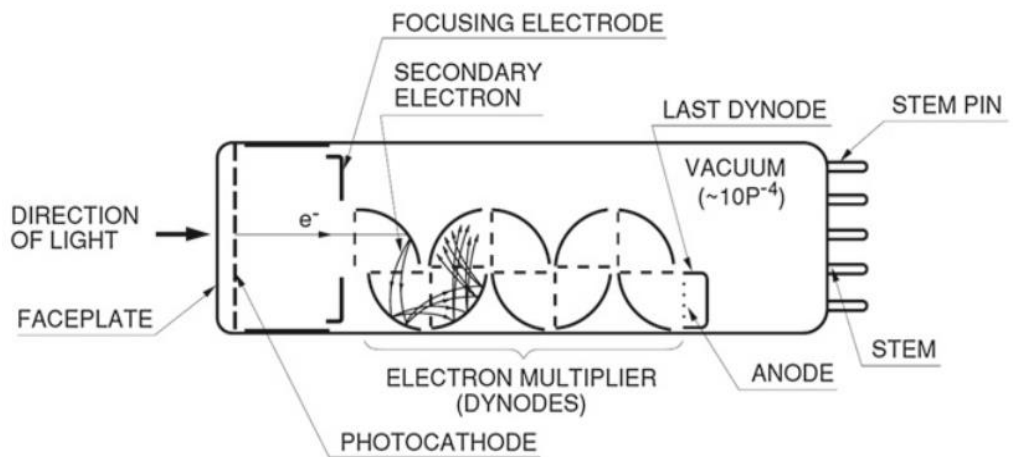


Figure 10: Schematic diagram of a typical photomultiplier tube and its components.⁵⁷

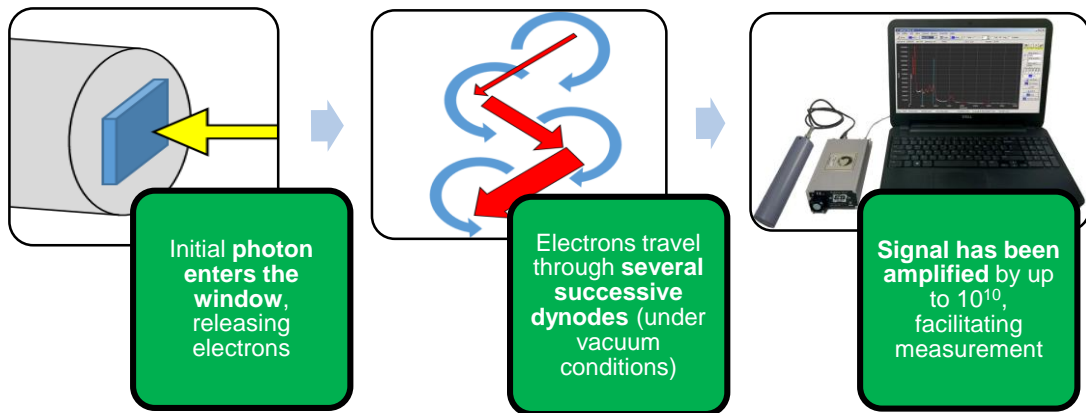


Figure 11: Photomultiplier tube operation principles.⁵⁸

1.5.2. Spectroscopy

In addition to measuring the amount of radiation in a post-accident scenario, the type of radioisotopes released must also be known. As shown in Table 5, there are several specific radioisotopes of concern given a typical CANDU reactor design and its potential failure modes. In order to identify which isotope is present, gamma spectroscopy can be used. In gamma spectroscopy, the inorganic scintillator detector systems utilize energy discrimination to place incoming radiation into energy bins, allowing for the resolution of energy spectra.

1.5.2.1. Radioisotopes

Each radioisotope undergoes a distinct mode of radioactive decay, causing the emitted radiation to be characteristic of the isotope. Specific radioisotopes of concern in the nuclear accident scenario include Cesium-134⁶⁰, Cesium-137⁶⁰, Iodine-131⁶⁰, and Cobalt-60⁶¹. As described in a CNSC study⁶⁰, ¹³⁴Cs, ¹³⁷Cs, and ¹³¹I can be hypothetically released from a CANDU nuclear power plant and be suspended in a radiological plume for up to 7 days. In addition to these isotopes, several others may also be present, however, for the purposes of this work, gaseous isotopes were not considered. While ⁶⁰Co is less likely to be found in the event of a nuclear accident, its consideration is important given the high energy gamma rays it emits and its accessibility for testing purposes. Henceforth, ¹³⁷Cs, ⁶⁰Co, and ⁵⁷Co will be discussed in depth as they were used to validate the spectrometry-based radioisotope identification component of the project.

Table 5: Estimated radionuclide release in previous nuclear accidents.⁶⁰

Isotope	Chernobyl (Bq)	Fukushima (Bq)
¹⁴⁰ Ba	2.5×10^{17}	3.1×10^{15}
¹³⁴ Cs	5.9×10^{16}	1.8×10^{16}
¹³⁷ Cs	8.2×10^{16}	1.5×10^{16}
¹⁴¹ Ce	2.0×10^{17}	1.8×10^{13}
¹⁴⁴ Ce	1.7×10^{18}	1.2×10^{13}
¹³¹ I	1.5×10^{18}	1.6×10^{17}
¹³² I	2.1×10^{18}	1.3×10^{13}
¹³³ I	3.0×10^{18}	4.2×10^{16}
¹³⁵ I	N/A	2.3×10^{15}
¹⁰³ Ru	2.3×10^{17}	7.5×10^9
¹⁰⁶ Ru	5.0×10^{16}	2.1×10^9
¹³³ Xe	6.0×10^{18}	1.1×10^{19}

¹³⁷Cs has a half-life of 30.07 years and can be produced by either nuclear fission, fast neutron activation, or thermal neutron activation. This radioisotope then goes on to decay into either ¹³⁷Ba directly (5.3%) via beta emission or into ^{137m}Ba which then goes onto decay into ¹³⁷Ba (94.7%).⁶² The less likely beta decay pathway results in the release of a 1.176 MeV beta particle while the second, more likely pathway results in the release of a 661.7 keV gamma ray. This 661.7 keV gamma ray can be clearly identified in the energy spectra generated by ¹³⁷Cs, since it is in secular equilibrium with ^{137m}Ba.

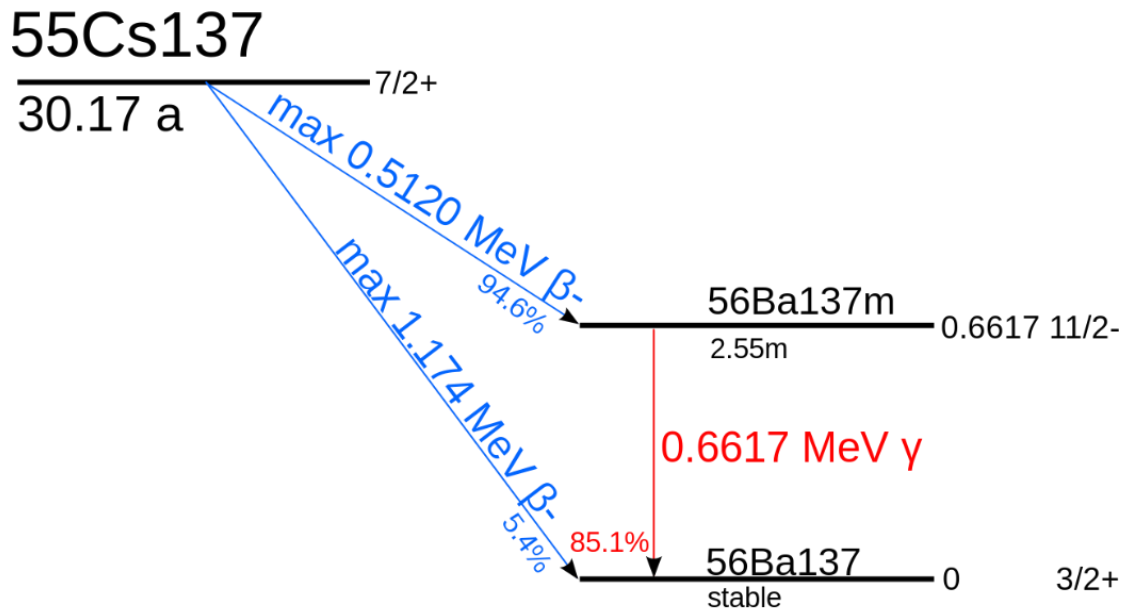


Figure 12: Decay scheme for ^{137}Cs into ^{137}Ba via beta decay.⁶³

The second isotope that will be expanded on and later analyzed in this work is ^{60}Co . ^{60}Co is a radioisotope that is generated synthetically in nuclear reactors and has use in the medical and sterilization industries. It has a half-life of 5.27 years and decays into ^{60}Ni via beta decay which then goes on to emit two high energy gamma rays as the activated nucleus de-excites. The decay scheme of ^{60}Co is shown in Figure 13.

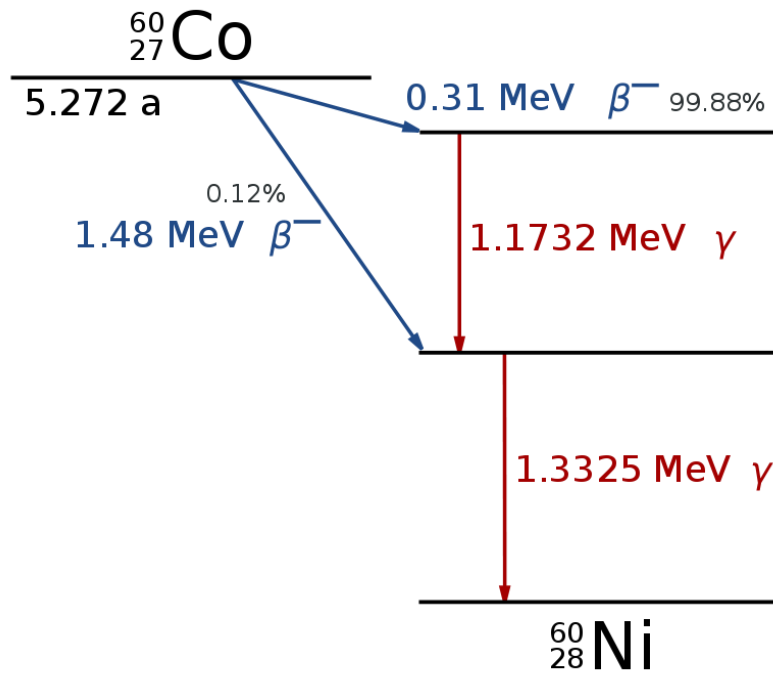


Figure 13: Decay scheme of ^{60}Co .⁶⁴

Finally, ^{57}Co is a radioactive isotope with many uses in healthcare. For example, it is used as a radioactive marker to allow physicians to quantify the absorption of Vitamin B₁₂.⁶⁵ Unlike ^{60}Co , ^{57}Co decays via electron capture, releasing three photons (122, 136, and 14 keV) and three beta particles (13, 115, and 130 keV). This radionuclide has a half-life of 272 days.⁶⁶

1.5.2.2. Measuring Energy Spectra

The energy spectrum of a radioisotope can be measured through the use of a scintillation detector coupled with a photomultiplier tube. As incident gamma rays from the radioisotopes being measured enters the scintillator's volume, visible light photons are

produced and converted into an amplified electrical signal via the PMT. The interaction phenomenon that enables spectroscopy is the photoelectric effect. As shown in Figure 14, the photoelectric effect is dominant at low energies and high atomic numbers, pair production is dominant at very high energies (greater than 10 MeV), and the Compton effect is dominant in the 0.5 to 5 MeV photon energy range.⁴⁶

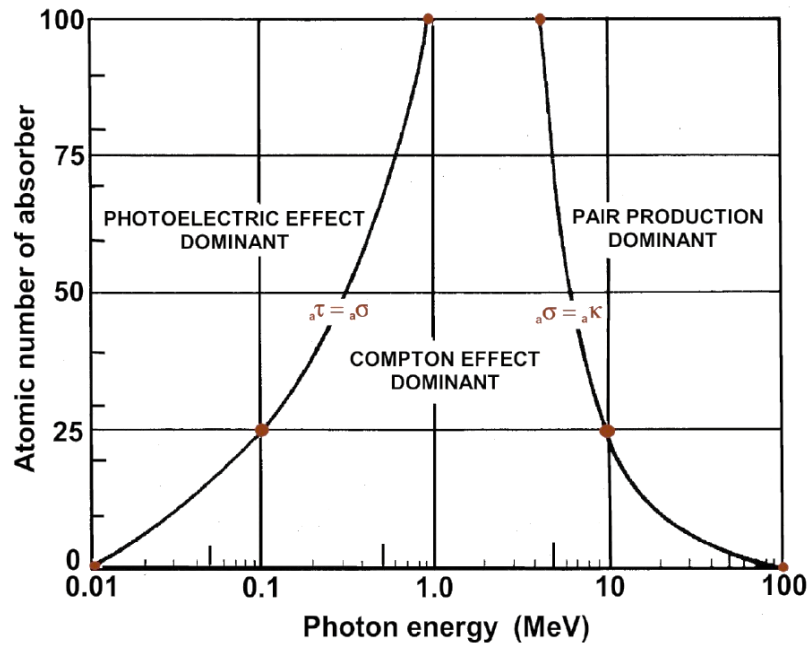


Figure 14: Photon interaction likelihood as a function of energy and the absorber's atomic number.²⁶

The photoelectric effect is when an incoming photon interacts with the target atom's orbital electron, ejecting it from its orbit. The vacancy created by the ejected orbital electron gets filled by an upper shell electron. The transition of this second electron to fill the vacancy results in the release of a photon with an energy equivalent to the difference between the two energy levels.^{46,66} This characteristic x-ray further undergoes its own

photoelectric interaction if in a high-Z material of sufficient thickness. Since the energy of the incoming photon is transferred entirely to electrons, the photoelectric effect coupled with inorganic scintillators make the ideal case for spectroscopy. As more electrons are produced and set into motion with greater energies, a proportionally large number of photons will be produced by the scintillator. This will then be amplified by the PMT and binned by a multichannel analyzer.⁴⁶

1.6. Use of Robotics in Nuclear Accidents

Research in the field of robotic systems for nuclear plant safety has been of interest for the past two decades. The main motivation behind incorporating robots into nuclear plant operations is to prevent humans from working in hazardous or dangerous environments. These robots could theoretically be controlled remotely, and information could be delivered to the plant operators and safety personnel in real-time.⁶⁷ Specifically, the goal of using these robots is to reduce the radiation dose and its harmful effects to workers. Interest in the use of robotics for nuclear accidents began after the Three Mile Island Incident in 1979, and again after the Chernobyl disaster in 1986. When the Fukushima accident occurred, there were several robots available for this purpose.³³ Early work on robotics in nuclear safety described machines that could clean in the event of a contaminant spill.⁶⁸ Other use cases included the decommissioning of power plants and passive monitoring of the plant environment.⁶⁹ Similar to other technology-based fields, robotics research has greatly accelerated in the past five years and rapid advances have been made. Figure 15 shows several generations of robots used in the nuclear setting.

Various groups are working on the use of other advanced techniques such as deep learning and computer vision in conjunction with robots, henceforth referred to as unmanned ground vehicles, or UGVs.⁷⁰ In addition to academic development, commercial stakeholders such as Boston Dynamics are constantly pushing the forefront of robotic development. The latest implementation of their work is the addition of ‘Spot’, a quadruped robot from Boston Dynamics, currently being tested for monitoring purposes at Ontario Power Generation (OPG; Figure 15(F)).

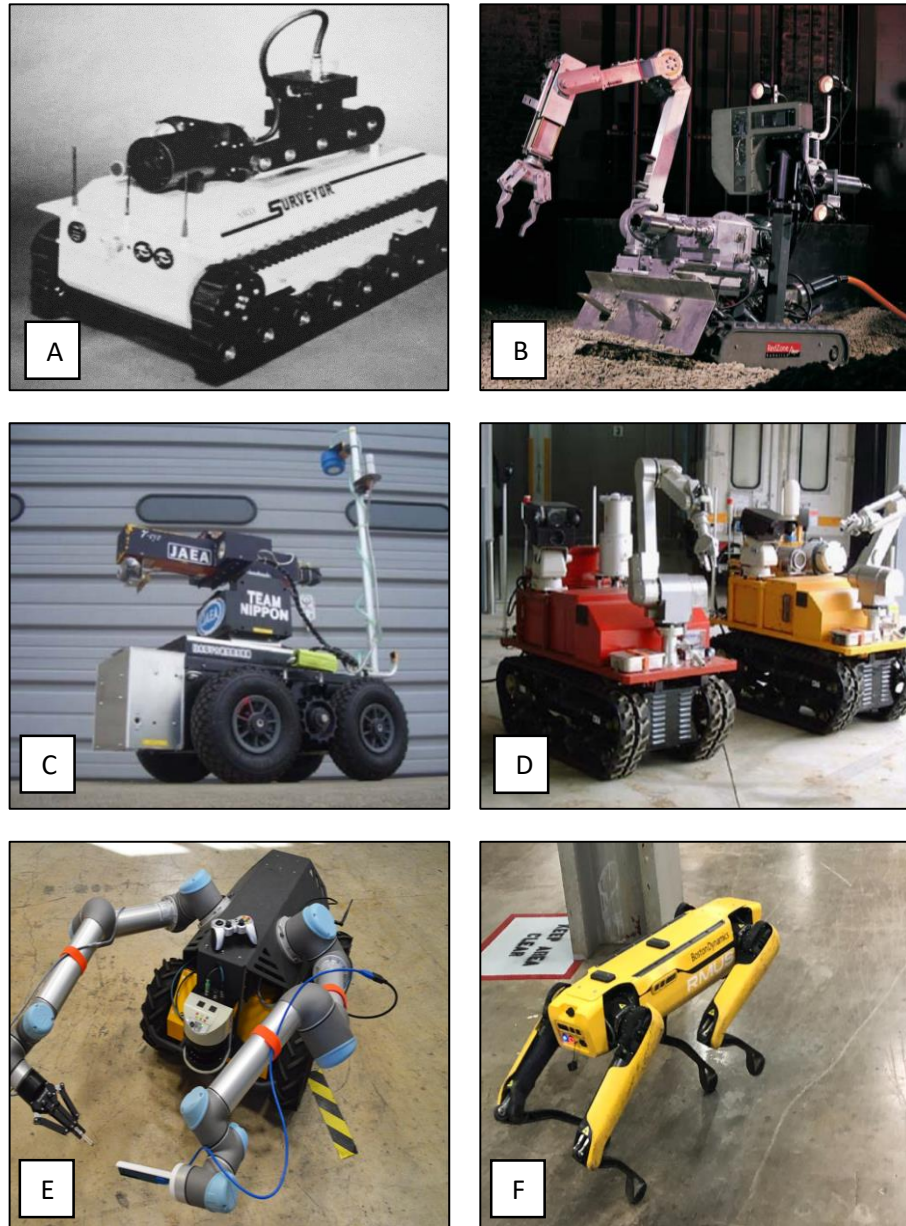


Figure 15: Ground based robotic systems from both past and present that have been used in nuclear settings. (A) is the ‘Surveyor bot’⁶⁷, (B) Pioneer 1¹ used for imaging inside of the Chernobyl sarcophagus, (C) JAEA Robot 3² for gamma ray imaging, (D) NUSTEC MoniROBO-A and B² used for infrastructure damage detection, (E) the VaultBot developed by researchers at the University of Texas Austin⁷¹, and (F) the Spot robot developed by Boston Dynamics currently used at Ontario Power Generation (OPG)⁷².

1.6.1. Radiation Mapping with Robotics

If the UGV technology described previously is equipped with sufficient radiation and air sampling machinery, a radiation map in a post-accident environment can be generated. Several groups have previously attempted to conduct radiation mapping using detector-equipped UGVs in order to localize sources of radiation.

Von Frankenberg et al. (2012) examined the early use of a mobile robotic platform to generate radiation maps.⁷³ Later, McDougall et al. (2018) conducted experiments with a fully functional, natively developed robotic platform to perform probabilistic mapping of radiation based upon sparse data.⁷⁴ Specific to the instrumentation used to perform these measurements, Miller et al. (2015) demonstrated the effectiveness of using inorganic scintillator-based detection on a mobile robot.⁷⁵ Specifically, they examined the use of LaBr₃ scintillator detectors for optimal surveying of gamma radiation sources in close proximity. Hosmar et al. developed a robot which could autonomously detect radiation and perform simultaneous localization and mapping (SLAM) within a defined polygonal area.⁷⁶ The combination of global positioning system (GPS) data with a NaI(Tl) scintillator detector allowed for source localization. This work was based on the particle swarm optimization algorithms. The UGV used in this work was the small and robust Clearpath Jackal.⁷⁷ In addition to this group, several others have been working on the optimization algorithms for source localization. Anderson et al.⁷⁸, used improved Bayesian inference methods to optimize radiation mapping using infrequent data points and then later improved upon their work to incorporate attenuation modelling methods.⁷⁹ Distinct from the NaI(Tl) and LaBr₃ methods described previously, another group attempted to use a cadmium zinc telluride semiconductor detector (CZT) paired with a CLYC (Cs₂LiYCl₆:Ce)

scintillator.⁸⁰ They placed these detectors on a UGV and were able to localize radiation sources in a simulated post-accident environment. Selivanova et al., also examined the use of CZT detectors with robotic systems and examined the use of a dual-armed robot.⁸¹ This group also used Monte Carlo simulation extensively to validate their configuration. Vetter et al., developed a technique known as scene-data fusion (SDF) that integrates LiDAR sensors and radiation detectors to produce 3D maps.⁸² They were then able to use these 3D maps in conjunction with computer vision. Similarly, another group was able to develop a three-pronged approach to map radiation field with multiple robots.⁸³ Their work utilized an unmanned aerial vehicle (UAV) for photogrammetry and aerial radiation mapping, and a UGV for ground radiation mapping. Finally, Ghawaly et al. mapped the results of a NaI(Tl) scintillator detector spectrum as they traversed an urban environment.⁸⁴ They then verified these results through measurement.

Additionally, robots that are not limited to the ground have also been utilized. Unmanned aerial vehicles (UAVs) have been previously explored for radiation mapping also. Jinlu et al. (2013)⁸⁵ explored the use of UAVs for radiation mapping in a post-accident scenario. Their simulation-based work focused on the platform, flight control, and cost effectiveness of the UAV platform. Similar studies were performed by other groups who explored the use of various detectors and spectrometers that would be optimal for a UAV system.⁸⁶⁻⁸⁸

1.7. Purpose and Specific Aims

As part of achieving the regulatory goals outlined in the severe accident management guidelines (SAMGs), the radiation doses and radioisotopes in the post-accident environment must be able to be accurately characterized. Particle size distributions must also be determined since the dose resulting from inhalation may be the largest contributing pathway in the early phases of an accident.⁸⁹ This must be done in order to ensure safety for emergency workers and members of the public. As described above, previous studies have explored the use of several UGV platforms for radiation detection. This project specifically focused on the integration of radiation measurement and air sampling devices onto a novel, superior UGV platform, the Husky A200 developed by Clearpath Robotics. Specifically, in this work, the optimal set of detector parameters for post-accident use were determined.

1.7.1. Specific Aims

- 1) Optimize detector parameters to be able to determine radiation dose as well as identify radioisotopes in a post-accident scenario.
- 2) Characterize detector stability and sensitivity to various scenarios.
- 3) Develop an algorithm for guiding emergency workers based on UGV detector data in the context of SAMGs.

2. Materials and Methods

This chapter discusses the main components of the robotic platform and the detector set used to characterize the radiation environment. In addition to this, the software development process will also be discussed.

2.1. Robotics Component

The unmanned ground vehicle (UGV) robot used in this study was the Clearpath Robotics (Kitchener, ON, Canada) Husky A200 UGV (Figure 16).⁹⁰ Previously, work was performed with other UGVs such as the natively developed ‘RadBot’⁷⁴ and the Clearpath Robotics Jackal.⁷⁷ In comparison, the Husky UGV has a larger on-board platform for mounting supplementary devices. In addition to this, the maximum payload in the Husky UGV was 75 kg, thrice the capacity of the Jackal UGV (20 kg). Additionally, the Husky also has a three-hour run time, stands 3.9 cm tall, and has a maximum speed of 1 meter per second. The on-board components of the Husky include a state-of-the-art LiDAR (light detection and ranging) system (the SICK LMS-211 2D), a Garmin GPS, as well as a router.

For on-board calculations and local control of devices, a supplementary laptop can be mounted. The Husky UGV is also capable of performing move-base navigation (basic autonomous planning and movement), simultaneous localization and mapping (SLAM), and adaptive Monte Carlo localization (AMCL). These features were not used in this study and are beyond the scope of this thesis.

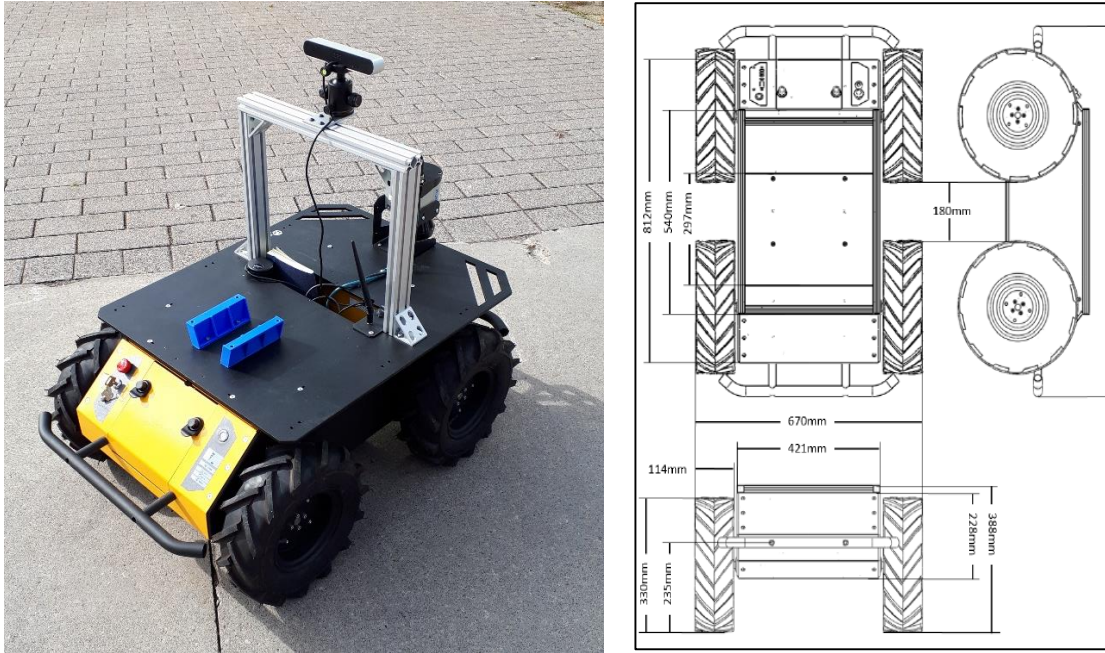


Figure 16: Husky UGV at the Ontario Tech University campus (left) and its schematic designs on the right.⁹⁰

Table 6: Husky UGV specifications.⁹⁰

Feature	Specification
Dimensions	990 × 670 × 390 mm ³
Weight	50 kg
Payload	Maximum: 75 kg All-terrain: 20 kg
Maximum speed	1.0 m/s
Clearance	130 mm
Operating ambient temperature	-10°C to 30°C
Operating time	3 hours active 8 hours standby
Battery type	24 V 20 Ah
Battery charge time	10 h

2.2. Characterizing Radiation Conditions

In order to measure the dose rate due to gamma radiation, the ThermoFisher RadEye G Gamma Survey meter was used.⁹¹ This handheld device is capable of measuring doses of up to 1,000 R. With regards to the dose rates, the RadEye is capable of measuring dose rates as low as 50 μ R per hour and as high as 10 R per hour. The energy range in which doses can be reliably (within 30%) measured ranges from 45 keV to 1.3 MeV. This device is also equipped with a Bluetooth Low Energy (BLE) Adapter which allows for the transfer of information via Bluetooth to a mobile device or computer.



Figure 17: ThermoFisher RadEye G Gamma Survey Meter. The image on the right shows the BLE adaptor at the back of the RadEye.

Table 7: Features of the ThermoFisher RadEye.⁹¹

Dimensions	9.6 cm x 3.1 cm x 6.1 cm
Weight	0.18 kg
Detection method	Geiger-Muller tube (energy compensated)
Detection range	0.5 μ Sv/h - 100 mSv/h
Energy range	45 keV - 3 MeV
Cs-137 (662 keV) count rate	1.7 cps per μ Sv/h
Battery	2 AAA batteries, 900 h life

2.2.1. Collection Time Optimization

Prior to mounting the RadEye onto the Husky UGV, the optimal parameters for the detector had to be determined. Of critical importance to the measurement of dose is the collection time. One of the modes of operation for the RadEye involves choosing between ‘Scaler mode’ and ‘Ratemeter mode’. The latter operates to provide a real-time estimate of the dose rate that updates every second, whereas the former provides a time-integrated dose rate measurement. Given that the RadEye is an energy compensated Geiger-Müller tube, a longer collection time using scalar mode would allow for more counts to be read by the detector and thus a more accurate measurement of the dose rate.

In this optimization experiment, several collection times were tested. These included 1, 5, 20, 40, 60, and 120 seconds; 50 readings were taken for each experiment. For all readings, the RadEye was kept at a fixed position, approximately 1 metre above the ground (Figure 17) in an open field in the Durham Region. These times were chosen to serve as a range between early, ideal, and long measurement times for the case of dose rate monitoring with the Husky UGV. Measuring for 1 second would seem too fast and likely to produce an inaccurate measurement, while measuring for 120 seconds may produce a more accurate and precise dose rate value, albeit for an impractical measurement time. The quantification of finding the right balance between speed of measurement and accuracy of results was the goal of this experiment.

All measurements were recorded, and appropriate statistical analysis were carried out using Microsoft Excel. These results can be seen in Figure 28 to Figure 33. The results generated here form the basis of the external dose assessment, as discussed in Section 2.4.



Figure 18: The handheld RadEye G⁹¹ experimental setup for 20 second dose rate collection time, 1 metre over the surface of the ground.

2.2.2. Isotope Identification

For identifying radionuclides through gamma spectroscopy, a Rexon GPS-200 2x2 NaI(Tl) scintillation detector is used in conjunction with the Universal Spectrum Analyzer (URSA-II) spectrum analyzer device (Figure 19 and 20), manufactured by S.E. International. Present radionuclides are identified using the accompanying multi-channel analyzer (MCA) software. It is important to note that gamma spectroscopy data from the URSA does not port directly to the SARC software, but the data files generated by the

URSA's Multi Channel Analyzer (MCA) software have a .usf file extension, which can be read in MATLAB as text (.txt) files.

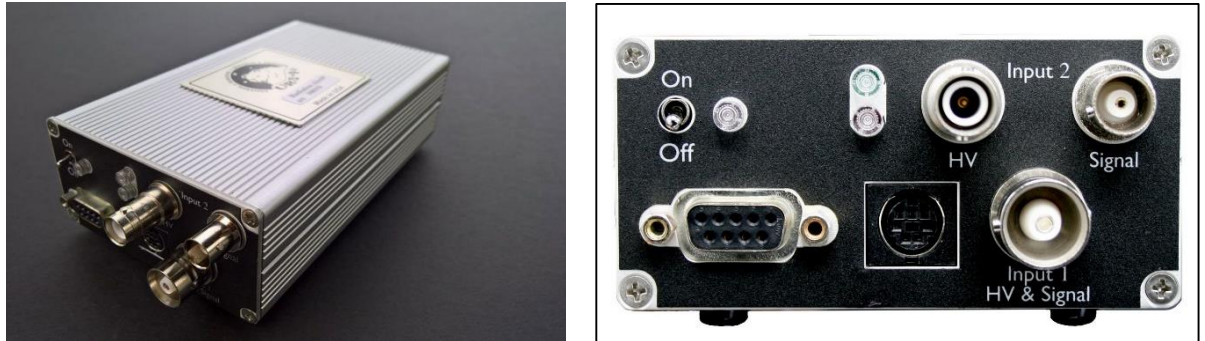


Figure 19: Universal Spectrum Analyzer (URSA)-II device which couples to the NaI(Tl) scintillator. Both the side view (left) and connections (right) are shown.



Figure 20: The measuring component of the setup. This casing contains the NaI(Tl) scintillator coupled to a photomultiplier tube using optical glue.

The principles of application of the spectroscopy system are described in the spectroscopy section in the introduction.

Due to detector malfunction and limited access to the laboratory, the URSA spectra files were provided by Steinmeyer, P. from Radiation Safety Associates, Inc. The raw files were used for the analysis in this project. Details of the measurement conditions and detector settings can be found in Table 8. As previously discussed, the two spectra used were: 1) ^{137}Cs spectrum, and 2) a mixed field spectrum consisting of peaks from ^{137}Cs , ^{60}Co , and ^{57}Co .

Table 8: Parameters from the NaI(Tl) spectra measurement. Spectra were obtained from Steinmeyer, P. from Radiation Safety Associates, Inc.

Parameter	^{137}Cs Measurement	Mixed Field Measurement
Manufacturer	Rexon	Rexon
Serial No.	0703-01	0703-01
Description	2×2 NaI(Tl)	2×2 NaI(Tl)
Cable length (in.)	36	36
Voltage (V)	950	950
Counting time (s)	600	1,800
URSA II MCA Version	2.0.18	2.0.18

2.3. Air Sampling

For severe accident conditions, it is also important to assess the weather conditions, as well as the air quality using air sampling equipment. More importantly, air quality monitoring equipment can be used to determine the air concentration of various radioisotope-sized particles, giving emergency workers a course estimation of contaminant

dispersion in air. The distribution of particle sizes can also allow for estimations to be made on internal dose as a result of inhalation.

To perform air sampling for particles of various sizes, the PurpleAir (or PA) SD-II Air Quality Sensor (PurpleAir; Draper, Utah) was used.³ The sensor is a small, stationary, and cost-effective device that can sample particles at sizes of 0.1, 0.3, 0.5, 1.0, 2.5, 5.0, and 10 micrometres, determine particle concentrations, and transmit data in real-time using Internet of Things (IoT) principles. This device is shown in Figure 21.



Figure 21: PurpleAir SD-II Air Quality Detector.³ On the left, the side view of the detector is shown while on the right, the two lasers used to measure air quality are shown.

The sensor is equipped with an internal SD card and two pre-calibrated Class 1 laser particle counters (PMS5003) for validating the data it collects against the other laser sensor. To begin using the sensor, it had to be registered on the PurpleAir cloud network, since the PA is an IoT device; the sensor collects and stores the air quality data in a cloud environment for the user to download. In remote areas where internet connectivity is unavailable (or if circumstances cause internet connection to be unavailable, like in severe

weather conditions), the data is stored in the internal SD card as a backup, and can be physically retrieved to access later.

Table 9: Features of the PurpleAir SD-II Sensor.⁹¹

Dimensions	8.5 cm x 8.5 cm x 12.5 cm
Weight	0.352 kg
Measurement method	Two laser particle counters (PMS5003)
Laser measurement range	0.3, 0.5, 1.0, 2.5, 5.0, 10 μm
Counting efficiency	50% (for 0.3 μm); 98% (for ≥ 0.5 μm)
Response time	≤ 1 s (single), ≤ 10 s (total)
Volume	0.1 L
Temperature range	-40°C - 85°C

The main benefit of this device is that it is a robust sensor capable of identifying many characteristics of the surrounding atmosphere, including weather conditions like temperature and humidity, while also providing health alerts when the concentration of particles reaches certain thresholds. Since it does not rely on batteries, the device can also collect data for long periods of time provided that it is connected to a power source; the PA used in this study collected data over many months.

2.3.1. PurpleAir Sensitivity Tests

The air sampler was placed in a fixed position outdoors and a particulate substance was directed towards the sensor for 30 second intervals for a total of 15 minutes (Figure 22). The sensitivity of the PA was tested using two different particulate substances: dust and talcum powder ($\text{Mg}_3\text{Si}_4\text{O}_{10}(\text{OH})_2$).

Dust was chosen as it contains several particulate sizes below 100 μm (typically present in sizes ranging from 1.0 to 100 μm) in diameter as well as a diverse set of constituents, as described by the National Institute of Standards and Technology in the USA.^{92,93} In this experiment, the dust used was collected over the period of 1 week from various indoor positions. Talcum powder was used given that it is present in particle sizes ranging from 0.3 to 100 μm , and has a median particulate diameter of 24 μm , which is close to the potential radioisotope particle diameters that would be measured in an accident scenario.⁹⁴

Of particular importance is the detection of particles below 10 μm in size, as this range is significant for internal dosimetry. Airborne radioactive particles at this size are considered respirable, as they are deposited into the deep lung, transported into the bloodstream and eventually deposited into tissue as energy, which is the absorbed dose quantity.

2.3.2. Long Term Stability Tests

In order to determine the PA's long-term stability, indoor measurements were taken daily for two months (March 4th, 2021, to May 1st 2021) with a 6-hour averaging time. The results were plotted and any trends were quantified.



Figure 22: Experimental setup of PurpleAir SD-II sensor. On the left, the device ID and barcode are redacted for privacy. On the right, the brightness of the image was increased to increase the visibility of the underside of the PA.

2.4. Development of Software Component

As mentioned previously, one of the main goals of this project was to develop a graphical user interface (GUI) software that can allow for the “data fusion” of the readings from the various detectors that would be integrated with the robotic platform. This would entail the readings of the multiple sensors to be displayed in the interface, along with visualizations to allow for easy interpretation of the data for a user located off-site.

To accomplish this, the first step was to choose an easy-to-use, flexible, and lightweight tool that would allow for the development of such a software. The initial choice was to develop the software using the Python programming language⁹⁵ and a combination of different Python libraries, namely Tkinter⁹⁶ to construct the software, and NumPy⁹⁷ and SciPy⁹⁸ for any calculations. A tentative script was constructed that was able to perform basic dosimetry calculations, but the main challenge in using Python was that it was

difficult to read and visualize the data from the sensors, which is ultimately the main purpose of the GUI. Additionally, any future steps taken to completely integrate the software with the Husky UGV (which runs on the Robot Operating System, or ROS) would be complicated since the integration of Tkinter with ROS was not found to be a straightforward process. Lastly, general computational and development issues like certain libraries not being installed or not being able to run on the native operating system caused increased difficulty in the continued development of the software. It was at this point that the Python interface was abandoned and MATLAB⁹⁹ was adopted as the software of choice.

Unlike Python, MATLAB has many powerful built-in libraries that can operate for any number of applications. This was the natural next choice due to its ability to communicate with ROS in different applications.⁹⁹ Also, MATLAB is a very powerful programming software that does not require any further installations on the part of the user (aside from the initial installation), thus allowing for smooth, uninterrupted development. Most importantly, the data from the three sensors was easily able to be read, displayed, and visualized in MATLAB.

2.4.1. Response Algorithm

The name given to the software is the ‘Severe Accident Radioactivity Classification’ software, or simply SARC. The main purpose of this software is to allow a user or operator located at an off-site location to be able to assess the radiological effects of a potential severe accident based on data collected and received from the sensors attached to the Husky UGV. Based on the sensors used, the user would be able to assess the gamma dose rate and classification of airborne radioactivity. As well, the user will be able to assess the dose levels to first responders located in the vicinity of the UGV based on classification of early, intermediate, and long-term effects as outlined by the ICRP in their report on large nuclear accidents.²¹.

The key features of this software and their development methods are outlined below by each of their respective tabs. The software algorithm is visualized in Figure 23, which shows the devices that are meant to be placed onto the Husky UGV, followed by their independent methods of transmitting data to the computer. Once the data files are received by the computer, they can be analyzed further in the SARC software.

Analysis performed in the SARC allows for a user to understand external and internal dose effects based on the data collected by the three detectors. The RadEye provides gamma dose rate values, while the air sampler, in conjunction with the URSA-II, allows for the rough estimation of internal dose resulting from inhalation.

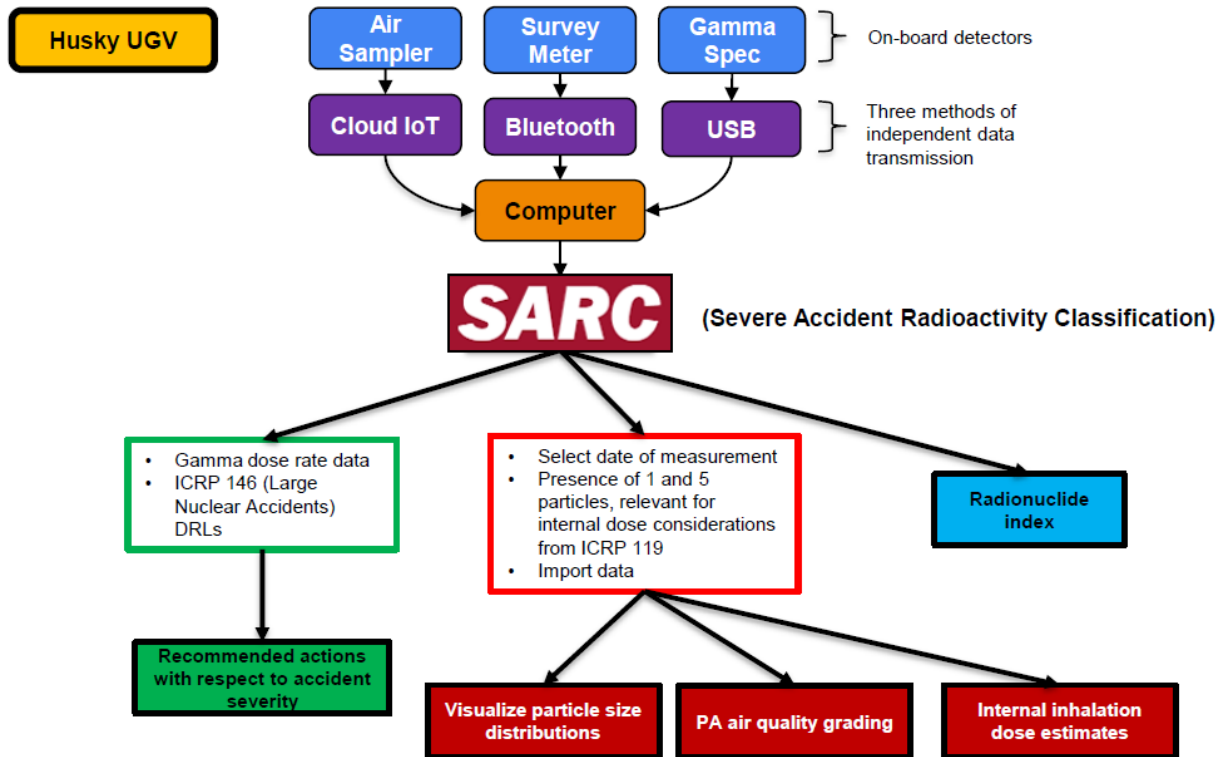


Figure 23: General workflow of the SARC software.

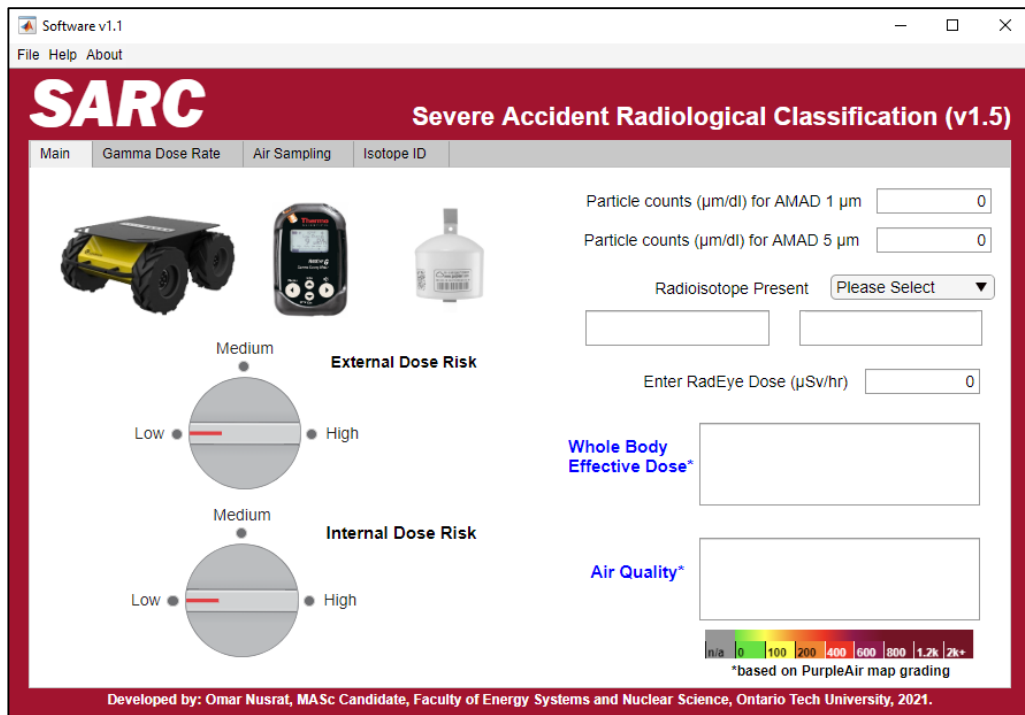


Figure 24: ‘Main’ tab of SARC software. Features include a quick estimate of air quality based on number of particles present and a quick estimate of effective dose based on dose rate of a selected radioisotope.

One major component of the SARC software is an alert system which notifies emergency workers of the danger levels based on the RadEye gamma dose rate measurements. This alert system triages the alert based upon the values given in ICRP 146.²¹ These risk levels are shown in Table 10. The values in green are what that specific category has been set to in the SARC software, within the defined bands and recommended limits from ICRP 146.

Table 10: SARC adaptation of ICRP 146 reference level limits by phase.

	Location	Early	Intermediate	Long-term
Responders	On-site	< 100 mSv Set to 250 mSv	< 100 mSv	< 20 mSv/year
	Off-site	< 100 mSv	< 20 mSv/year	1-20 mSv/year Set to 5 mSv per year
Public	Off-site	< 100 mSv		1-20 mSv/year Set to 2 mSv per year

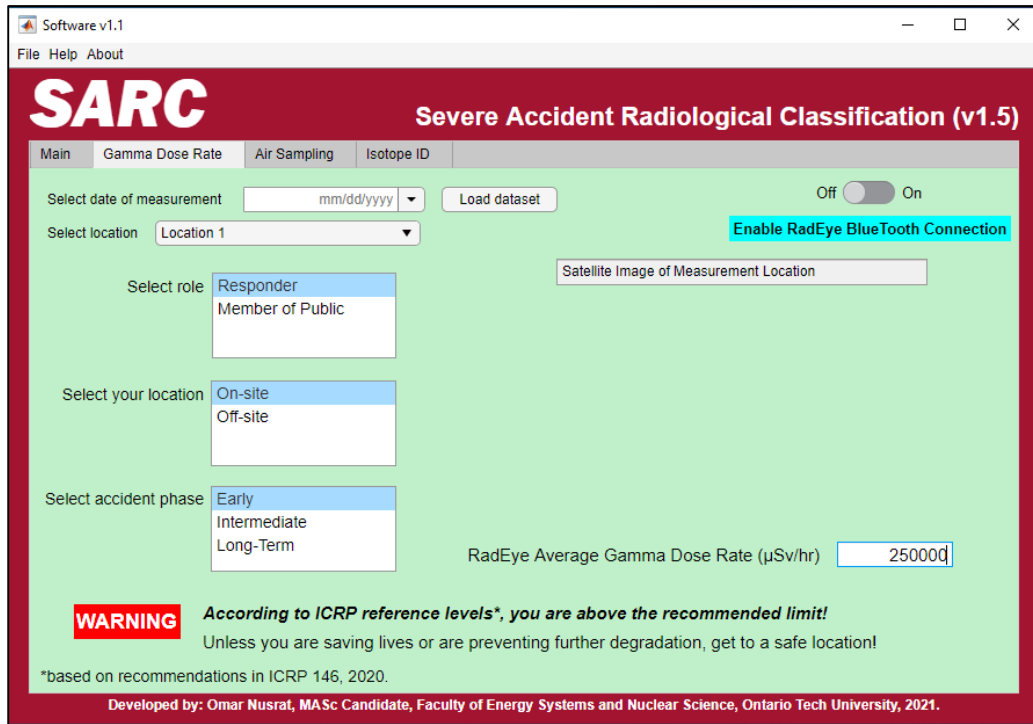


Figure 25: ‘Gamma Dose Rate’ tab of SARC software.

Users can select from a set of locations to have a map appear with the dose locations and their respective dose rates. The user can also select their role as either a ‘Responder’ or ‘Member of the Public’; dose reference levels (DRLs) from ICRP 146 will then advise the user on recommended actions.

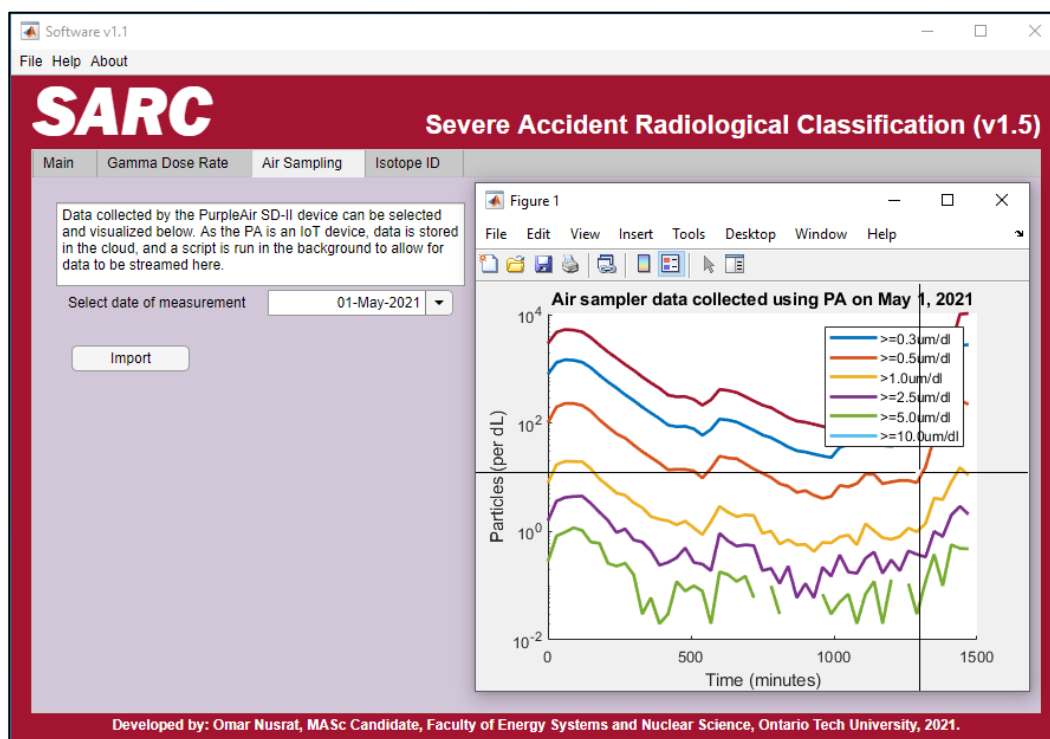


Figure 26: ‘Air Sampling’ tab in SARC. Data collected by the PurpleAir sensor can be loaded and visualized here.

As depicted in Figure 26, the user can load and visualize data collected by the PA sensor as a size distribution based on the date of collection. Currently the software loads data for 10 and 60 minute averaging times.

As can be seen in Figure 27, the user is able to select the present radioisotopes based on the spectrum data from the URSA-II MCA software, and can find out important information of said radionuclide.

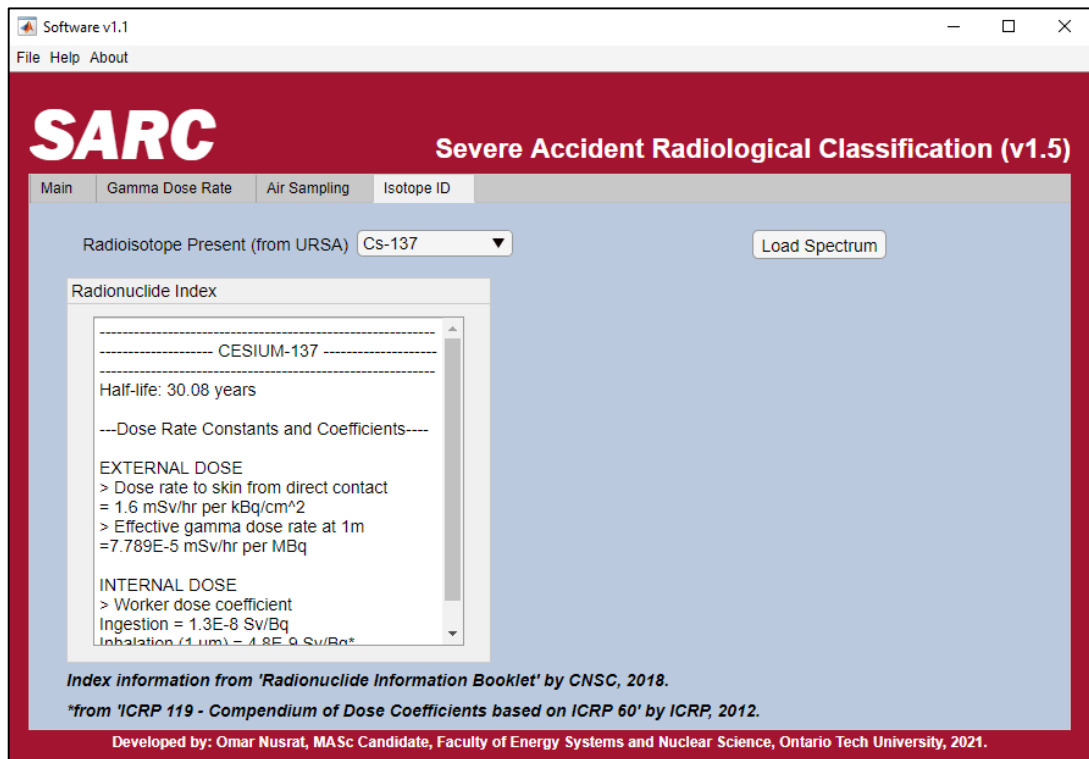


Figure 27: 'Isotope ID' tab in SARC.

3. Results

The results obtained from the different experiments performed during this project are outlined in this section. These can be categorized as results obtained for optimizing dose rate measurement times with the RadEye G Gamma Survey Meter, and results for determining the long-term stability and sensitivity of the PurpleAir Sensor.

3.1. Dose Rate Measurements

The dose rate measurements described here were made against background radiation; no external sources were used in these experiments. The reasons for this are outlined in the Discussion section.

3.1.1. Collection Time Optimization

In this section, the collection time on the RadEye dose rate measurement function was optimized. For each collection time interval, 50 readings were taken. The mean and standard deviation for each case was quantified.

The dose rate measured for a 1 second collection time can be seen in Figure 28. The error bars correspond to the standard deviation of the mean. It is clear by the variation in the measured data points that the 1 second collection time does not provide a stable, average dose rate value over 50 readings.

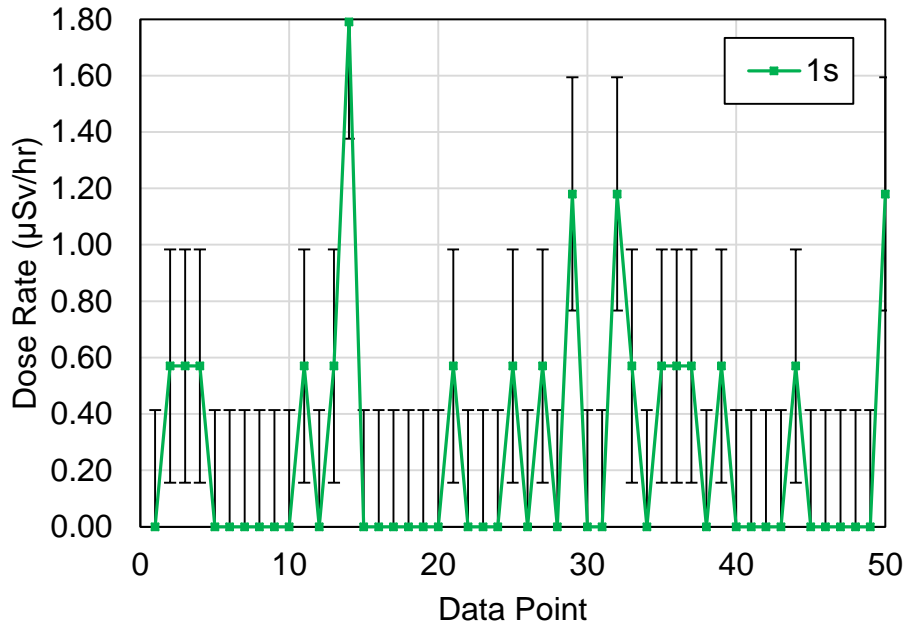


Figure 28: Dose rate measured using 1 s collection time on the RadEye detector.

In Figures 29 to 33, the dose rate was determined for collection times of 5, 20, 40, 60, and 120 seconds. It is clear that an increased collection time is directly proportional to an increased collection time (seen in Table 11), as the stability of the results is at its highest for a 120 second collection time dataset, seen in Figure 33. However, despite providing the most stable dose rate results, it is also impractical in a real-life severe accident scenario for the Husky UGV to spend this long collecting one data point. Since this is too long, a shorter collection time like 20 seconds seems more practical, especially due to a relatively low standard deviation in measurements, as seen in Table 11.

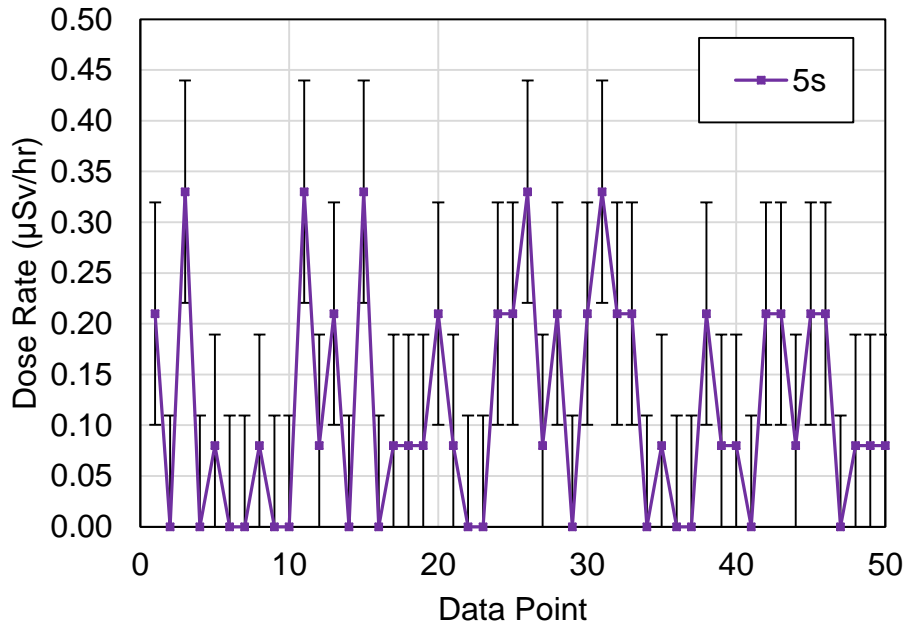


Figure 29: Dose rate measured using 5 s collection time on the RadEye detector.

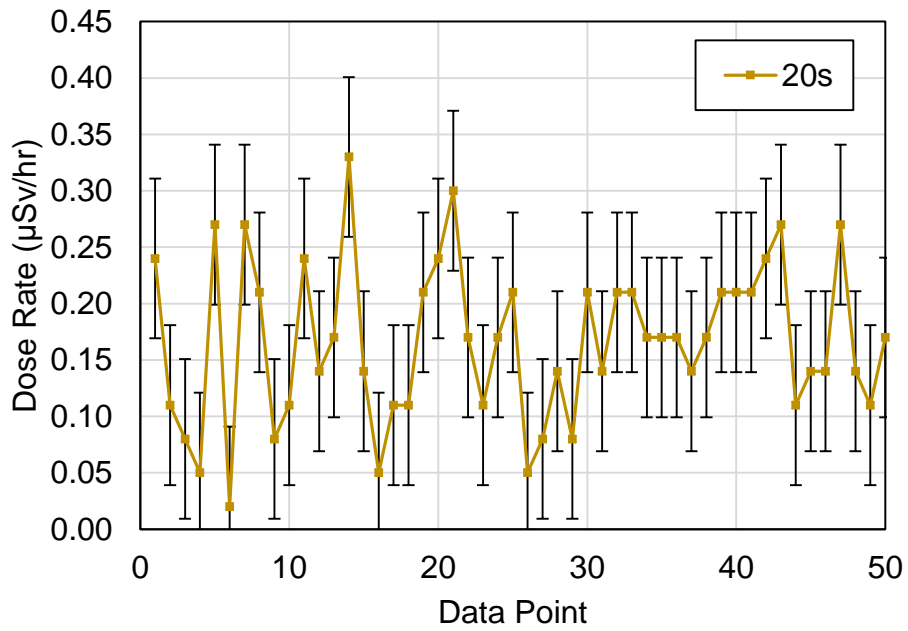


Figure 30: Dose rate measured using 20 s collection time on the RadEye detector.

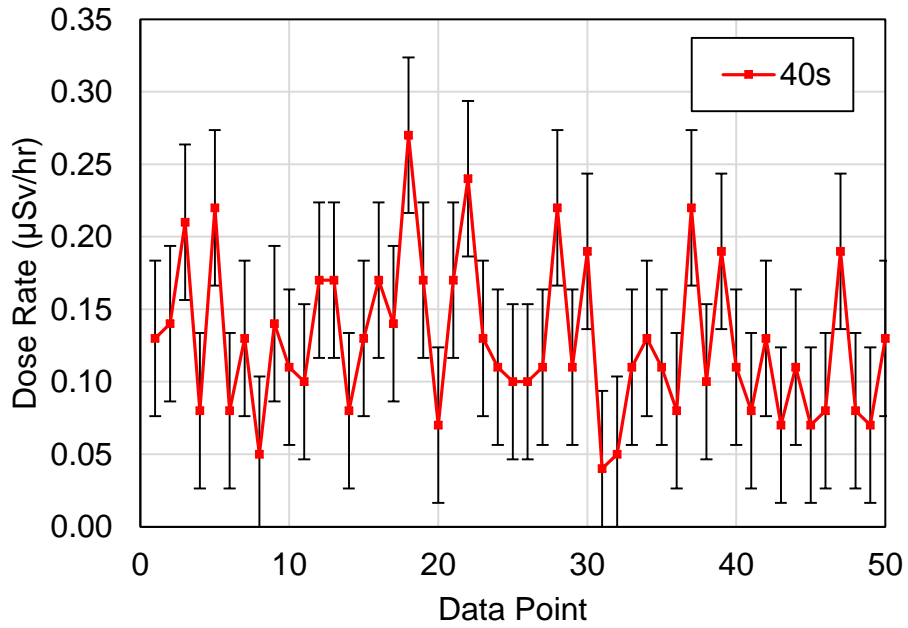


Figure 31: Dose rate measured using 40 s collection time on the RadEye detector.

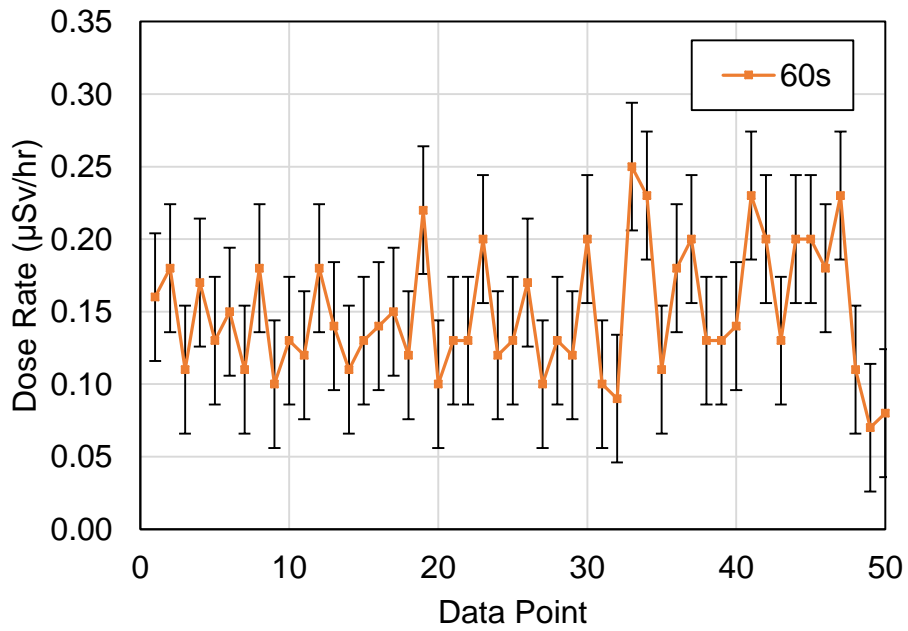


Figure 32: Dose rate measured using 60 s collection time on the RadEye detector.

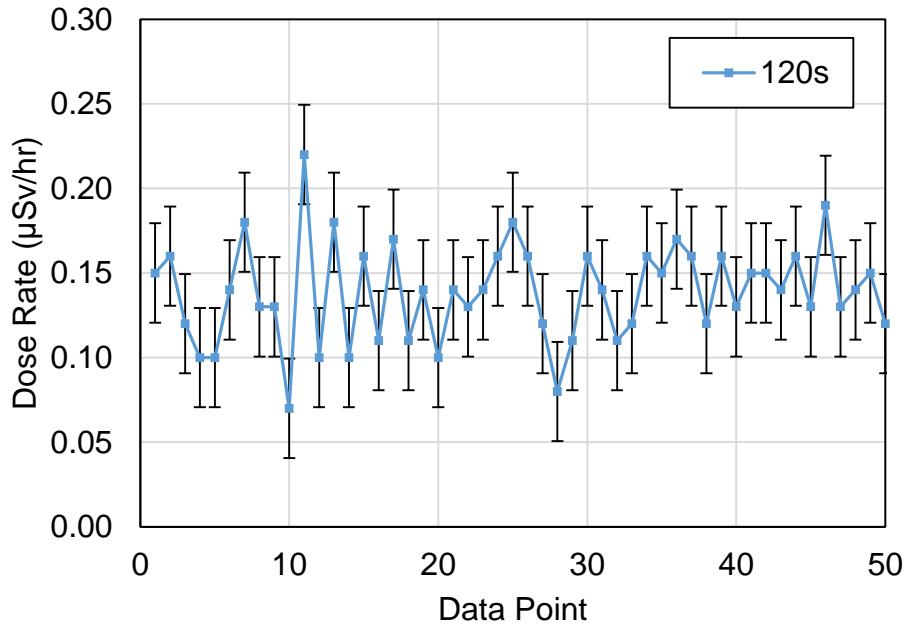


Figure 33: Dose rate measured using 120 s collection time on the RadEye detector.

Table 11: Mean and standard deviations for each collection time interval tested.

Collection Time (s)	Mean Dose Rate (\bar{D} ; $\mu\text{Sv/hr}$)	Standard Deviation (σ ; $\mu\text{Sv/hr}$)	Standard Deviation (% of \bar{D})
1	0.27	0.41	155%
5	0.17	0.11	95%
20	0.17	0.071	43%
40	0.13	0.054	42%
60	0.15	0.044	30%
120	0.14	0.029	21%

Table 12: Comparison with natural background measurement in the Greater Toronto Area (GTA).

	Annual Dose Rate	Hourly Dose Rate
Background dose in GTA ¹⁰⁰	1.59 mSv/yr	0.182 μ Sv/hr
Measured dose (20 s)	1.49 mSv/yr (\pm 0.6 mSv/yr)	0.17 μ Sv/hr (\pm 0.07 μ Sv/hr)
Absolute Difference	0.10 mSv	-
% Difference	6.7%	-

In Table 12, the dose rate measurements made with the RadEye were compared to background radiation data reported by the CNSC¹⁰⁰. Since the RadEye was operated in the Durham Region, the data was compared to the reported background annual dose rate value for the Greater Toronto Area. The comparison shows that there was only a 6.7% difference between the reported and experimentally obtained values for a 20 second collection time.

3.2. Isotope Identification

In this section, two radioisotope samples were examined. Due to technical difficulties with the NaI(Tl) detector, spectra collected by the manufacturer were used for the analysis component. As described in the methods section, two samples were measured. The first sample was a ^{137}Cs spectra, while the second was a mixed field spectrum consisting of ^{137}Cs , ^{60}Co , and ^{57}Co . The URSA software allows for the user to specify the channel and peak energies for the energy calibration. For both spectra, the energy calibration plots are shown in Figures 34 and 37. For ^{137}Cs , the two peak energies used were the full energy peak of 661.7 keV and 32.89 keV.

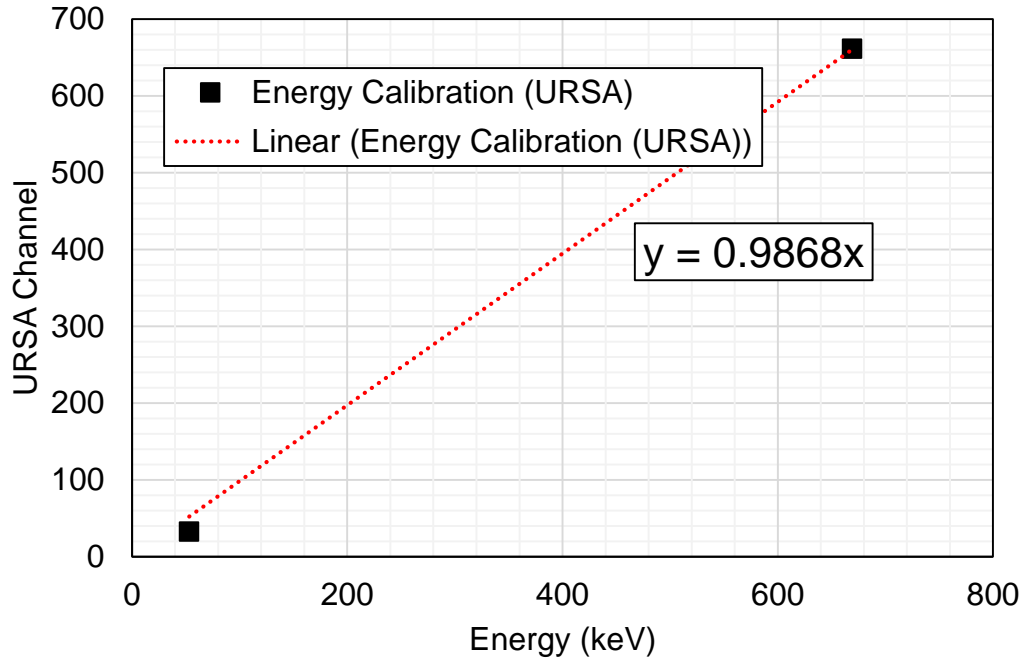


Figure 34: Channel-to-energy calibration for the ^{137}Cs used in the URSA analysis software.

The two ^{137}Cs energies correspond to the 661.7 keV and 32.98 keV peaks. The slope of this plot (0.9868 keV per channel) was used to convert the spectra from channel binned to energy binned as shown in Figures 35 and 36. The calibration to energy is generally the product of the gain and channel plus the offset.

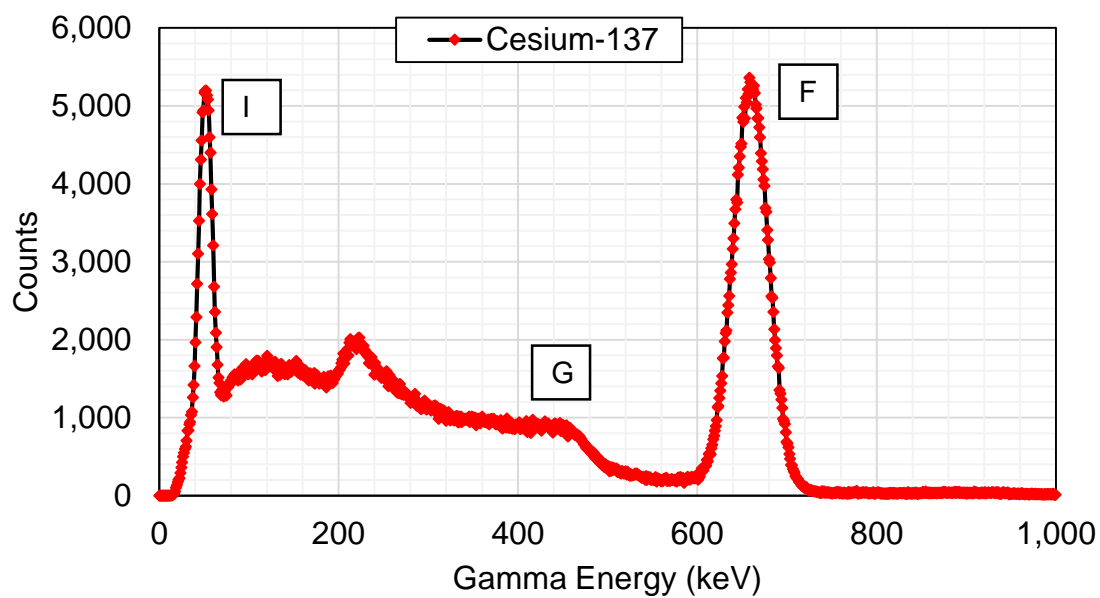


Figure 35: Energy spectra for ^{137}Cs measured using the URSA NaI(Tl) detector and analyzed using the URSA software. Data provided by Steinmeyer, P. from Radiation Safety Associates, Inc. Peak labels correspond to Table 13.

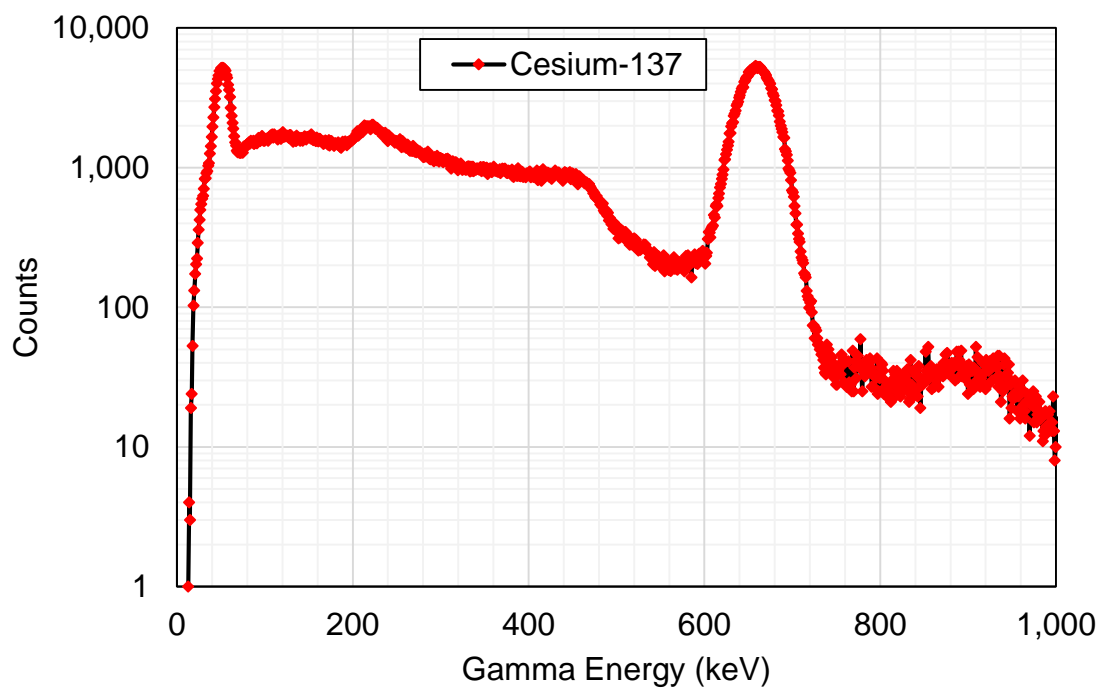


Figure 36: Energy spectra for ^{137}Cs measured using the URSA NaI(Tl) detector and analyzed using the URSA software shown with the y-axis in the logarithmic scale.

Data provided by Steinmeyer, P. from Radiation Safety Associates, Inc.

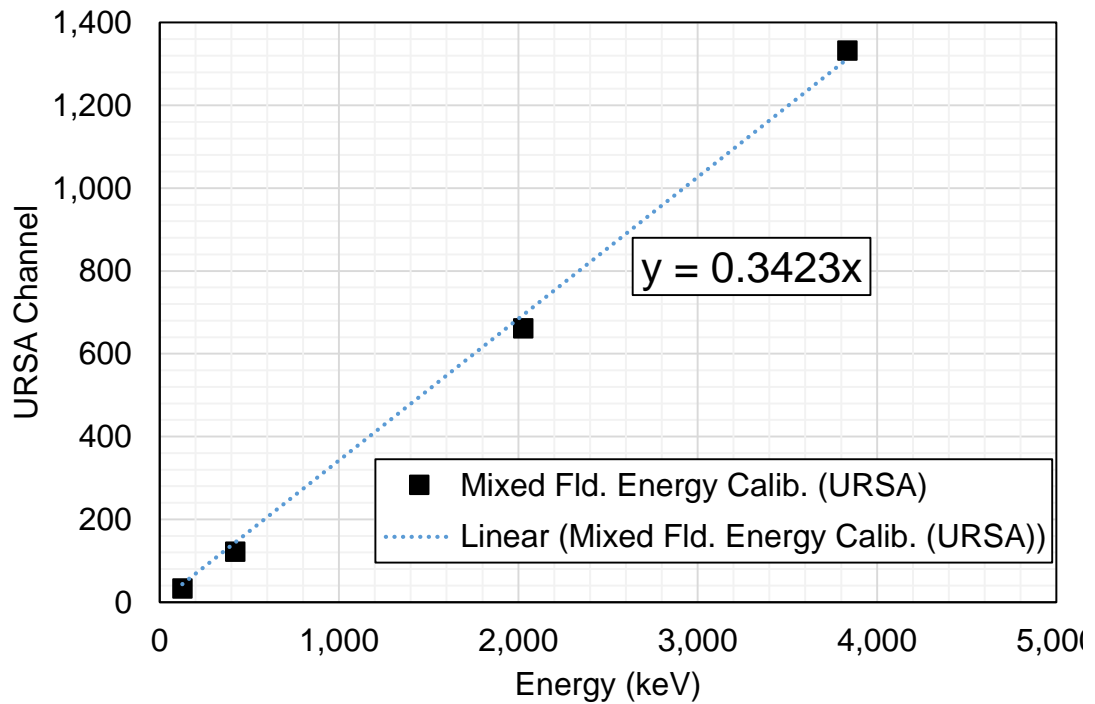


Figure 37: Channel-to-energy calibration for the mixed field data used in the URSA analysis software.

The energy points correspond to the two from ^{137}Cs (661.7 and 32.98 keV), one from ^{60}Co (1332.5 keV), and one from ^{57}Co (122.06 keV). The slope of this plot (0.3423 keV per channel) was used to convert the spectra from channel binned to energy binned as shown in Figures 38 and 39.

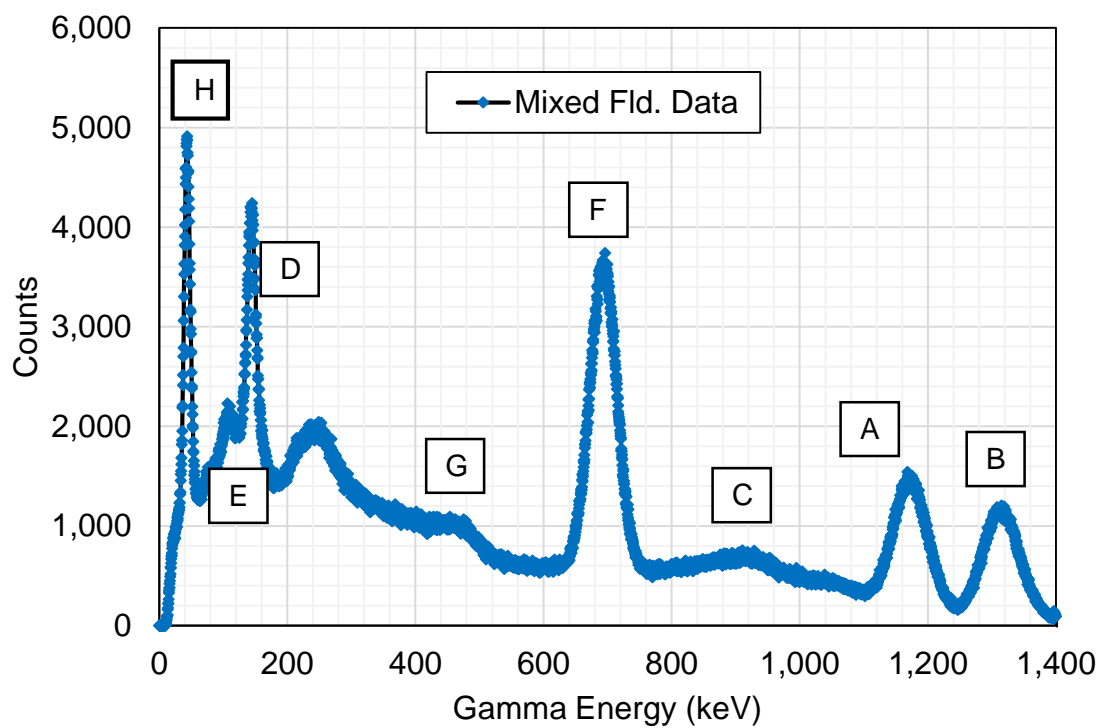


Figure 38: Energy spectra for the mixed field measured using the URSA NaI(Tl) detector and analyzed using the URSA software. Data provided by Steinmeyer, P. from Radiation Safety Associates, Inc.

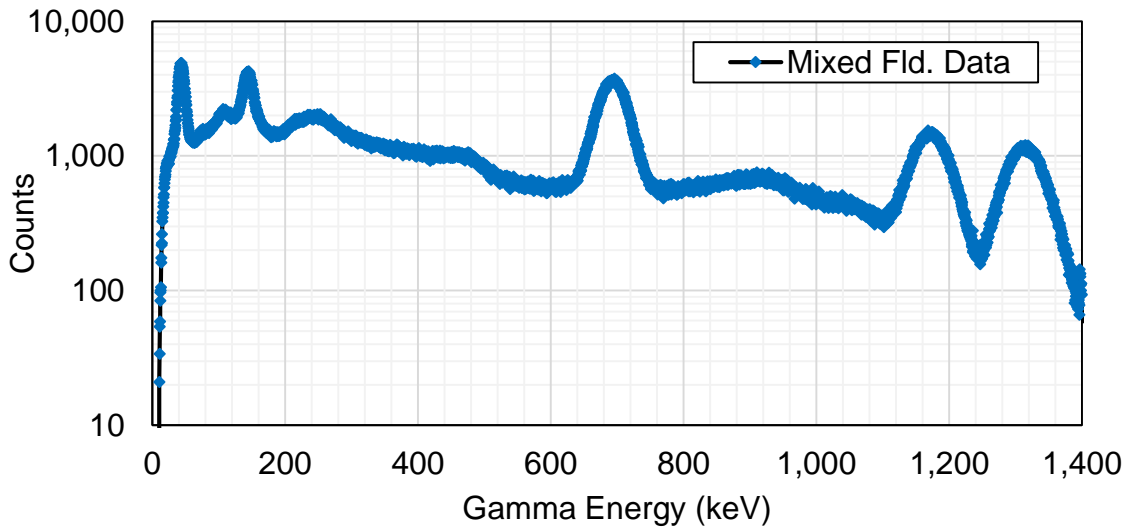


Figure 39: Energy spectra for the mixed field measured using the URSA NaI(Tl) detector and analyzed using the URSA software shown with the y-axis in the logarithmic scale. Data provided by Steinmeyer, P. from Radiation Safety Associates, Inc.

Table 13: Identification of all peaks in the ^{60}Co , ^{57}Co , and ^{137}Cs spectra shown in Figures 35, 36, 38, and 39.

Peak	Isotope	Energy	Description
A	^{60}Co	1.17 MeV	Full energy peaks are centred at approximately 1.17 and 1.33 MeV. These values agree with the decay scheme of ^{60}Co . These incident gamma rays completely dissipate their energy to charged particles in the scintillator which creates light corresponding to the incoming energy. ¹⁰¹
B		1.33 MeV	

C		0.89 MeV	Compton edge which is the maximum energy of the scattered electrons. When the initial gamma ray collides with and scatters an electron through the Compton effect. A portion of these scattered electrons also go on to produce light in the scintillator. In order to verify this, the energy of the Compton edge can be calculated and is shown below.
D	^{57}Co	0.13 MeV	Full energy peaks of ^{57}Co centred at approximately 0.122 and 0.136 MeV according to the ^{57}Co decay scheme. ¹⁰¹
E		0.14 MeV	
F	^{137}Cs	0.66 MeV	Full energy peak of ^{137}Cs .
G		0.46 MeV	Compton edge: caused by the ^{137}Cs photons that undergo the Compton effect and produce light inside the scintillator. The calculation to validate the measurement is shown below.
H		0.033 MeV	^{137}Cs decays into ^{137}Ba , which has a K_{α} mean transition energy of 32.89 keV. ¹⁰¹

Compton Edge Calculation

In this calculation, the theoretical energy of the Compton edge for both ^{137}Cs and ^{60}Co was calculated. This is done by utilizing the formula for the Compton wavelength shift post photon-electron collision⁴⁶:

$$\Delta\lambda = \frac{h}{m_0c}(1 - \cos\theta) \quad (2)$$

^{60}Co Compton Edge Calculation

In this calculation, the theoretical energy of the Compton edge for both ^{137}Cs and ^{60}Co was calculated. This is done by utilizing the formula for the Compton wavelength shift post photon-electron collision⁴⁶:

$$\begin{aligned} \Delta\lambda &= \frac{h}{m_0c}(1 - \cos\theta) \\ \lambda_f &= \lambda_i + \frac{h}{m_0c}(1 - \cos\theta) \end{aligned} \quad (3)$$

The maximum energy transferred to the scattered electron and therefore lost by the gamma ray occurs when $\theta = 180^\circ$,

$$\lambda_f = \lambda_i + \frac{h}{m_0c}(1 - \cos 180^\circ)$$

$$\lambda_f = \lambda_i + \frac{h}{m_0c}(2)$$

$$\lambda_f = \frac{1240}{E}nm + \frac{hc}{m_0c^2}(2)$$

$$\lambda_{f,1.17} = 0.0010598nm + \frac{2(1240eV * nm)}{511eV}$$

$$\lambda_{f,1.17} = 0.00596 \text{ nm}$$

$$E_{f,1.17} = 208,000 \text{ eV} = 0.208 \text{ MeV}$$

$$E_{\text{electron}} = 1.17 \text{ MeV} - 0.208 \text{ MeV} = \mathbf{0.962 \text{ MeV}}$$

For the 1.33 MeV gamma ray,

$$\lambda_{f,1.33} = 0.00093233 \text{ nm} + \frac{2(1240 \text{ eV} * \text{ nm})}{511 \text{ eV}}$$

$$\lambda_{f,1.33} = 0.005832 \text{ nm}$$

$$E_{f,1.33} = 213,000 \text{ eV} = 0.213 \text{ MeV}$$

$$E_{\text{electron}} = 1.33 \text{ MeV} - 0.213 \text{ MeV} = \mathbf{1.18 \text{ MeV}}$$

¹³⁷Cs Compton Edge Calculation

$$\Delta\lambda = \frac{h}{m_0c} (1 - \cos\theta)$$

$$\lambda_f = \lambda_i + \frac{h}{m_0c} (1 - \cos\theta)$$

The maximum energy transferred to the scattered electron and therefore lost by the gamma ray occurs when $\theta = 180^\circ$,

$$\lambda_f = \lambda_i + \frac{h}{m_0c} (1 - \cos 180^\circ)$$

$$\lambda_f = \lambda_i + \frac{h}{m_0 c} \quad (2)$$

$$\lambda_f = \frac{1240}{660,000 eV} nm + \frac{hc}{m_0 c^2} \quad (2)$$

$$\lambda_f = 0.001879 nm + \frac{2(1240 eV * nm)}{511 eV}$$

$$\lambda_f = 0.00678 nm$$

$$E_{f,PHOTON} = 183,000 eV = 0.18 MeV$$

$$E_{electron} = 0.66 MeV - 0.18 MeV = \mathbf{0.48 MeV}$$

Table 14: Spectroscopy parameters. Dead time could not be obtained as the spectra were obtained from Steinmeyer, P. from Radiation Safety Associates, Inc.

	¹³⁷ Cs	Mixed Field
Collection Time	600 s	1,800 s
Estimated Dead Time	N/A	N/A
Voltage	950 V	950 V
Energy Conversion	0.9868 keV/channel	0.3423 keV/channel
Total Counts	971,539	4,329,138

3.3. Air Sampling

Outlined here are the results obtained through two sets of experiments performed with the PurpleAir SD-II Air Quality Sensor, or 'PA'. The first experiment examined the PA stability over measuring air samples over a long period of time, and the second set of experiments examined the sensitivity of the PA to determine various particle sizes, ranging from 0.3 to 10 μm , which are the relevant ranges for internal dose effects resulting from inhalation.

3.3.1. PurpleAir Stability over Time

As mentioned, the first experiment examined the stability of the PA in measuring and collecting air samples over a long period of time. This is an important parameter to consider, especially when comparing the differences in air quality from before and after occurrences of incidents where a plume may or may not be present for a given period of time. In this case, the PA sampled air from March 4th, 2021 to May 1st, 2021 to determine whether the air quality was stable in a controlled outdoor environment. Figure 40 depicts the number of particles of size 1 and 5 μm sampled per decalitre with the PA over the given timeframe, with a 6-hour average sampling time.

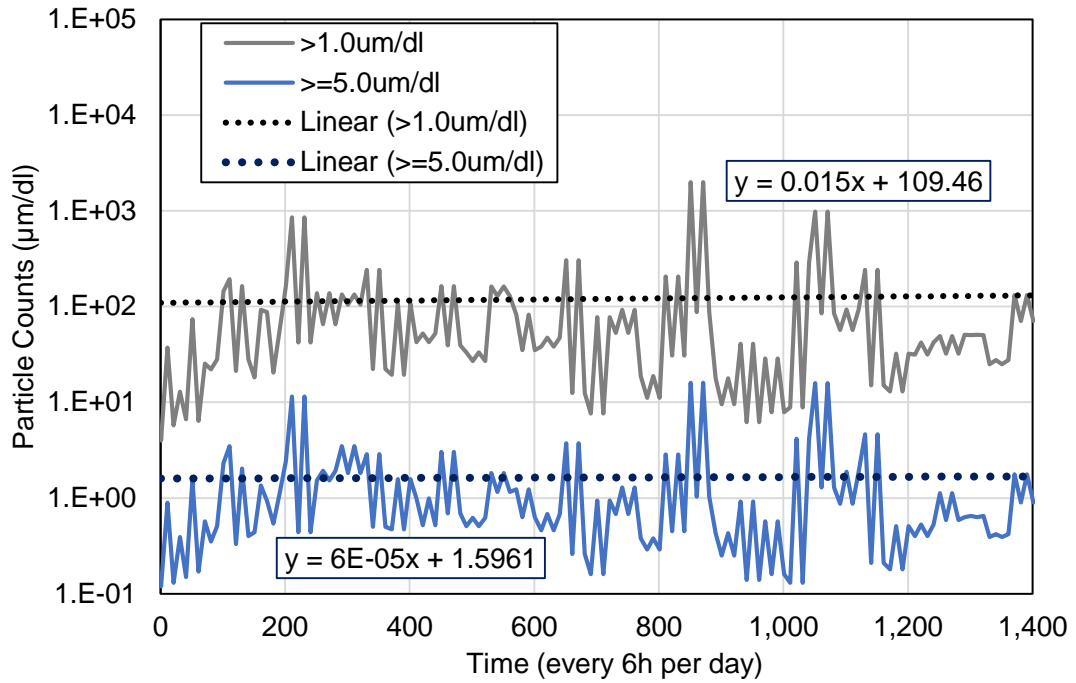


Figure 40: Stability of PurpleAir measurement over the course of two months (March 4th 2021 to May 1st 2021) with a 6 hour averaging time.

As can be seen from Figure 40, the slopes of the fit lines for both 1 and 5 µm are nearly zero, providing strong evidence that the PA is a suitable device for long term air sampling due to the stability of sampling results produced from close to two months of continuous measurements.

3.3.2. Sensitivity Analysis

The results of the sensitivity analysis of the PA device are shown in Figure 41. Sensitivity was determined with respect to the ability of the PA to effectively discriminate sampled air particles based on particle sizes of 0.3, 0.5, 1.0, 2.5, 5.0, and 10.0 μm . While this can be determined through passive sampling (i.e. allowing the PA to passively sample particles in its surrounding environment), the goal here was to mimic the air quality conditions following a severe accident. To do this, non-radioactive particle stimulants, namely talcum powder and dust, were sprayed in the direction of the PA to assess its sampling ability.

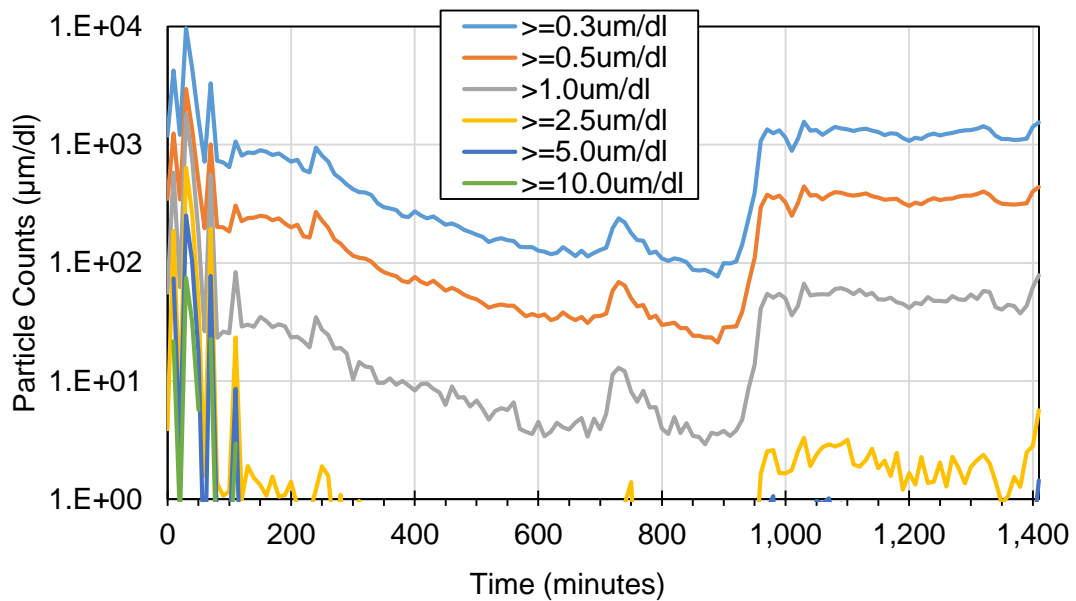


Figure 41: Air sampler data collected using the PurpleAir device after talcum powder exposure for several particulate sizes including: 0.3, 0.5, 1.0, 2.5, 5.0, and 10.0 μm .

The data shown here was collected using 10-minute collection times as described in the Methods section. Two minutes after collection began, the PurpleAir device was exposed to a plume of talcum powder.

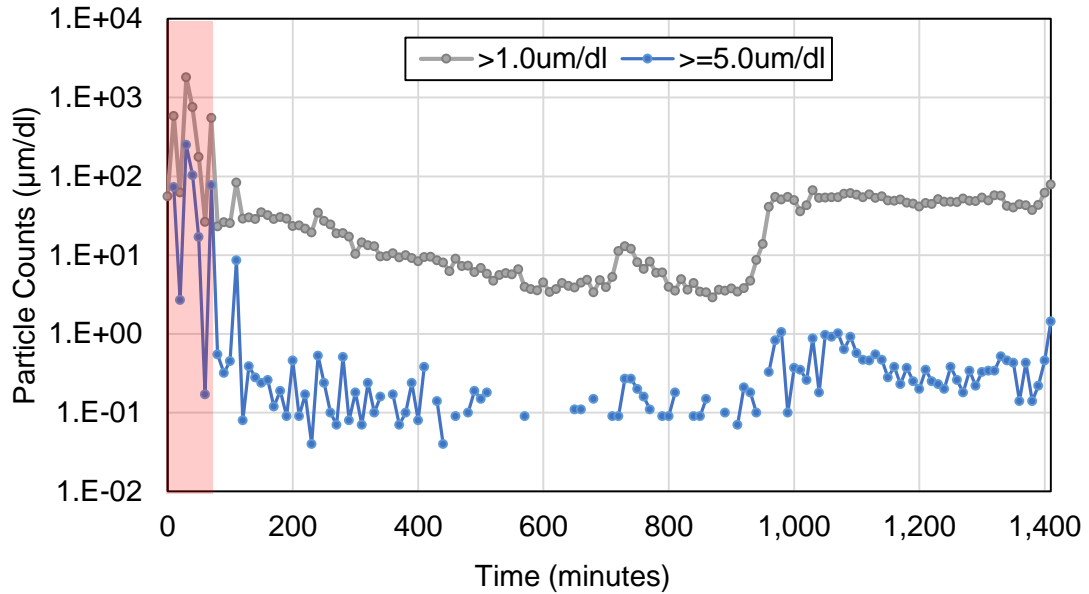


Figure 42: Air sampler data collected using the PurpleAir device after talcum powder exposure for particles of size 1.0 and 5.0 µm sampled per dl.

The results for 1 and 5 µm sampled per decalitre are explicitly shown because these two particulate matter sizes have the most significance in the nuclear accident setting with regards to inhalation dose, according to ICRP 119.¹⁰² The data shown in Figure 42 was collected using 10-minute collection times as described earlier. Two minutes after collection began, the PurpleAir device was exposed to a plume of talcum powder (shown in red).

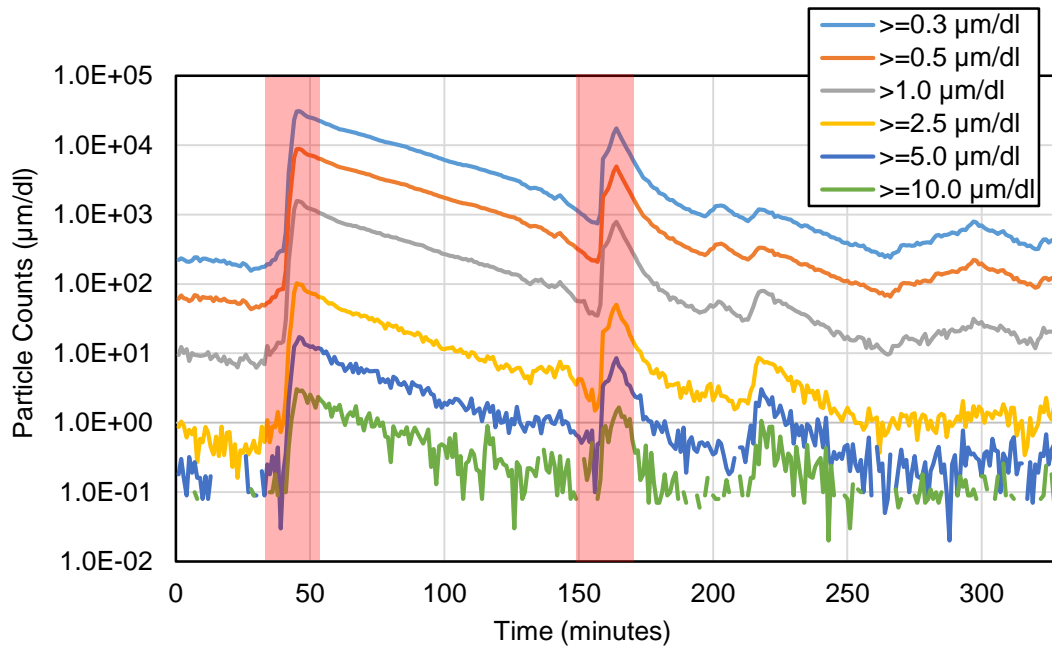


Figure 43: Air sampler data collected using the PurpleAir device after dust exposure for several particulate sizes including: 0.3, 0.5, 1.0, 2.5, 5.0, and 10.0 μm particles per dl.

The data shown in Figure 43 was collected using 10-minute collection times as described in the Methods section. Two minutes after collection began, the PurpleAir device was exposed to a plume of dust.

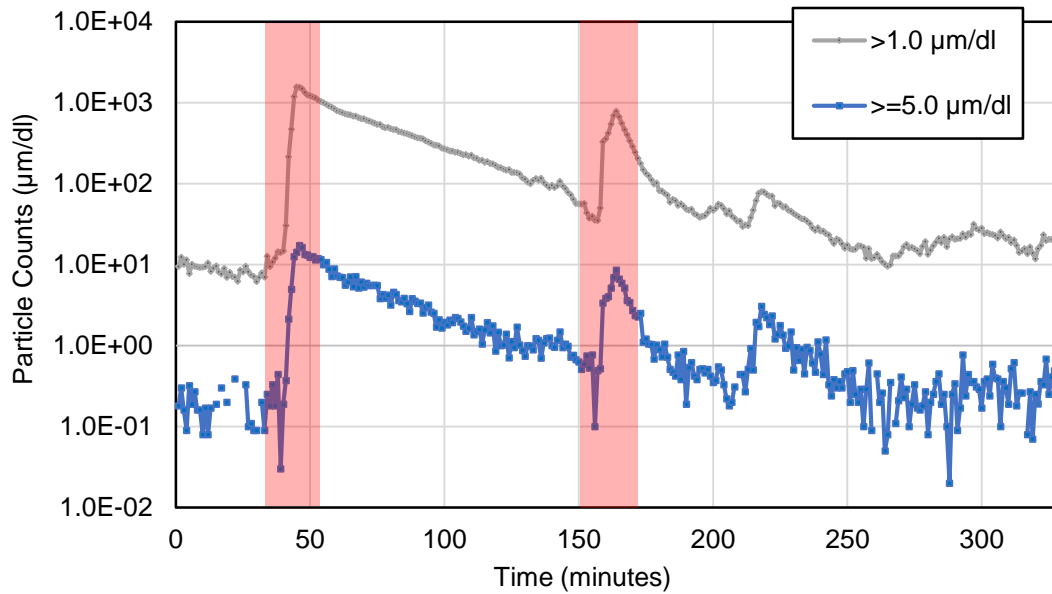


Figure 44: Air sampler data collected using the PurpleAir device after dust exposure for several particulate sizes including: 1.0 and 5.0µm sampled per dl.

Seen in Figure 44 is the same data seen in Figure 43, but isolating for particles of size 1 and 5 µm, which are relevant for internal dosimetry. The exposure incidents are highlighted in red.

4. Discussion

The purpose of these experiments was to determine the optimal detector parameters and sensitivities for a specific detector set aiming to measure dose rate, identify radionuclides, and characterize airborne radioactivity for robotic applications in severe accident scenarios. This was achieved by performing experiments that optimized the collection time of the RadEye G Gamma Survey Meter, tested the PA Air Sampler's sensitivity and long-term stability, and by developing software that is able to read, visualize, and process data from the multiple sensors used.

Since the specific application of these devices was for severe accident management purposes, certain regulatory equipment qualifications were considered with the instrumentation used.¹⁰³ These involved considering equipment based on their suitability to perform the intended functions, and their capability to withstand external hazards, electromagnetic disturbances, and the potential harsh environmental conditions following an accident scenario. One of the most important aspects of assessing equipment for reliable performance is the environmental profile¹⁰³, which looks at certain parameters as a function of time that results from severe accident conditions. For example, radiation profiles can be generated in the form of dose rate versus time; similarly, the air quality can be measured as a function of time, which has been an objective of this work that has been met with the experiments conducted.

The IAEA technical document titled 'Assessment of Equipment Capability to Perform Reliably under Severe Accident Conditions' mandates that the assessment of equipment capabilities under severe accident conditions must consider certain factors. The

availability, accessibility, and functionality of all instruments needs to be ascertained. In the case of the detector set that was examined in this study, all three aspects were relatively easy to quantify. The devices examined are all available for public use and purchase, and are made easily accessible due to their respective sizes and ease-of-use with regards to data and software. Finally, they all serve the required purpose with regards to functionality by effectively measuring the desired parameters in the conditions they were tested in. In addition to this, the other factors that the IAEA discussed in their report included: uncertainty in loading instrument parameters, location of equipment, and electrical performance of the equipment under harsh considerations.

According to Canadian regulations³⁴, one of the requirements for plant operating licensees is the development of an accident management program. Within this program, they must utilize instruments that can ‘obtain information, as necessary, on key parameters’ which include temperatures and radiation levels, both of which can be sensed by the PA and RadEye, respectively.^{3,34,91} It must also be demonstrated ‘with reasonable assurance that the equipment and instruments used in severe accident management will survive and perform their intended functions in the ensuing harsh conditions’. The PurpleAir, RadEye, and Husky UGV are designed to be highly robust and to maintain operations in very harsh weather conditions, however, with regards to the PA, there have not been other uses in the literature for nuclear applications. To that end, further research is required in radiation effects, hardening, and survivability of the Husky and the PA sensor. Additionally, the robustness of the NaI(Tl) scintillator detector used in this work has not been examined.

4.1. Radiation Measurements

In this work, the RadEye G Gamma Survey Meter was used to measure the dose rate at a given point. Given that the RadEye is an energy compensated Geiger-Müller detector, longer collection times would allow for more accurate and precise measurements of dose rate.^{46,66} However, in the context of its use in this work, longer collection times would mean that the fully-equipped Husky UGV would be stationary for a prolonged period of time. This would prevent it from being able to quickly map and assess the entire area and would be a futile use of limited battery resources.

Considering these limitations, several collection times were examined. These time periods included 1, 5, 20, 40, 60, and 120 seconds. As shown in Table 10, the standard deviation across different collection times varied greatly. For the shortest collection time of 1 second, the standard deviation is 155.4%. This reduced to 21% for the 120 second collection time. The mean dose rates and standard deviations for all collection times greater than 1 second did not vary significantly. In order to balance UGV positional stagnancy and accurate dose rate measurement, a collection time of 20 seconds was determined to be ideal.

In Table 12, the measured dose rates are compared to the background radiation dose rates as determined by the CNSC.¹⁰⁰ The tabulated background radiation dose rate in the Greater Toronto Area is 1.59 mSv per year. In this work, the measured background dose rate was found to be 1.49 mSv per year (± 0.6 mSv per year). This dose rate was measured using a 20 second collection time. The measurement in this work was approximately 6.7% less than the CNSC tabulated value. There may be several reasons for this discrepancy.

Firstly, the RadEye detector contains a small active collection volume, potentially leading to large variations in measurement. Next, the measurements taken in this work were done in Durham Region, Ontario, approximately 30 minutes from downtown Toronto. Slight variations in altitude and environmental conditions may also explain this discrepancy.

As mentioned by the IAEA¹⁰³, the response time of an instrument used in an accident response scenario must be considered in the context of the original function of the instrument. In this case, a 20 second collection time will be associated with relatively large (up to 43%) variation, however, given the UGV's function and the response time post-accident, this is an acceptable characteristic.

In a study from Brookhaven National Laboratory¹⁰⁴, the RadEye Personal Radiation Detector (PRD) and PRD-Extended Range (PRD-ER) models were deemed as appropriate devices for monitoring and surveying in what the USA's National Council on Radiation Protection and Measurements¹⁰⁵ (NCRP) defines as the Cold Zone. The cold zone is where the dose rate is below 10 mR per hour, since that is the maximum measuring range of the device (specific to the PRD). It stands to reason that the RadEye G, given that it has a maximum measuring range of 10 R per hour, would be suitable for radiation surveying use in the Cold Zone and the Hot Zone (exposure rate less than 10 mR per hour), but not in the Dangerous Radiation Zone (DRZ) where the exposure rate exceeds the 10 R per hour limit of the RadEye G. Therefore, based on regulatory requirements¹⁰⁶ for accident management instrumentation, the RadEye is a suitable device for monitoring in areas where the dose rate does not exceed 10 R per hour, or 100 mSv per hour.

4.2. Spectroscopy Results

As previously explained, due to detector issues and COVID-19, spectroscopy measurements were not taken, however, two measured spectra were used for the analysis and software validation in this work (courtesy of P. Steinmeyer from Radiation Safety Associates, Inc.). It was known that first spectra corresponded to a ^{137}Cs source, while the second corresponded to a mixed field measurement of ^{137}Cs , ^{57}Co , and ^{60}Co . The energy to channel calibration for both spectra are shown in Figure 34 and 37. These were done using the full energy peaks from each of the isotopes examined. The URSA software is capable of doing this internally, however, this was done in order to validate the software. This was especially important considering the originally planned integration of the spectra results into the SARC MATLAB code. The spectra for both are shown in Figures 35 and 38 in the results section. The origin of each of the peaks are outlined in Table 13 and the position of the ^{137}Cs and ^{60}Co Compton edges were verified mathematically.

Both measurements were done using a high voltage of 950 V; the collection times were 600 s and 1800 s for ^{137}Cs and ^{60}Co , respectively. These relatively short spectroscopy time periods are appropriate in the post-accident context of the project.

4.3. Air Sampling Measurements

As previously described, air sampling measurements were conducted using the PurpleAir system. There were two main tests in the air sampling section: 1) long term stability, and 2) sensitivity to different particulate types. In the first experiment, the PurpleAir was used to measure 1 and 5 μm particulate matter twice daily for two months

(Figure 40). For the second component, two sample materials were used in the sensitivity tests: dust and talcum powder. Dust was ideal for use because it contains several particulate diameters and material compositions (both organic and inorganic). According to the National Institute of Standards and Technology (NIST), both urban and indoor (general) dust contains particulate matter smaller than 100 μm .^{92,93} Talcum powder was also used because it was comprised of a uniform material composition and had a medium particle diameter of 24 μm .⁹⁴

As shown in Figure 40, the long-term stability of both the 1 and 5 μm particulate matter measured using the PurpleAir was quantified. Over two months, the linear line of best fit indicated that there was an increase of 0.015 counts per day for the 1.0 μm size and an increase of 6.0×10^{-5} counts per day for the 5.0 μm particles. This slight trend upwards is largely negligible and may be attributed to natural changes in air quality as the seasons changed from winter to spring. In order to fully assess stability, measurements would have to be taken for the full year to understand natural environmental changes and how it compares to the PA stability.

Figures 41 and 42 show the PA's sensitivity when exposed to plume of talcum powder. As can be seen, there was a large reading after exposure with a steady decline until approximately the 1,000 minute mark. At this point, all particulate matter readings increased uniformly. This may be explained by either a movement in the PA's position or orientation, or possibly a change in the ventilation of the room in which the PA was housed when placed indoors. When exposed to dust (twice; Figures 43 and 44), there was a sharp immediate increase followed by a steady decline as expected. Based on this, the PA can be said to be sensitive to particle sizes relevant in a nuclear accident scenario. There are two

major downsides to the PA device. First, the minimum reading time is 10 minutes. If the UGV is moving at high speeds, a measurement of air quality after 10 minutes may make it difficult to localize the position of high particulate (of interest) concentrations. Secondly, the PA requires an internet connection for real-time monitoring to function. In a post-accident scenario, there may be significant infrastructure damage which may render the PA useless due to power outages. More robust connectivity for the PA must be explored, including Bluetooth or USB-based connections.

As mentioned earlier, the particle size distribution data gathered by the PA can be used to make internal dose estimations as a result of inhalation based on particle size-dependent dose conversion factors (DCFs).^{66,102} This can be done using the DCFs outlined in ICRP documentation¹⁰² (see Table A.1 in Appendix) for 1 and 5 μm , or by generating DCFs based on larger particle sizes in a program like IMBA.¹⁰⁷ The DCF is dependent on particle size since the diameter determines the region of deposition within the respiratory tract, which in turn, influences the dose received due to inhalation. For example, a higher percentage of larger particles deposit in the upper airway, whereas smaller particles are generally deposited in the deep lung.¹⁰⁸

The data collected from each of the instruments can be used to make estimations of internal and external dose, as shown in the figure below.

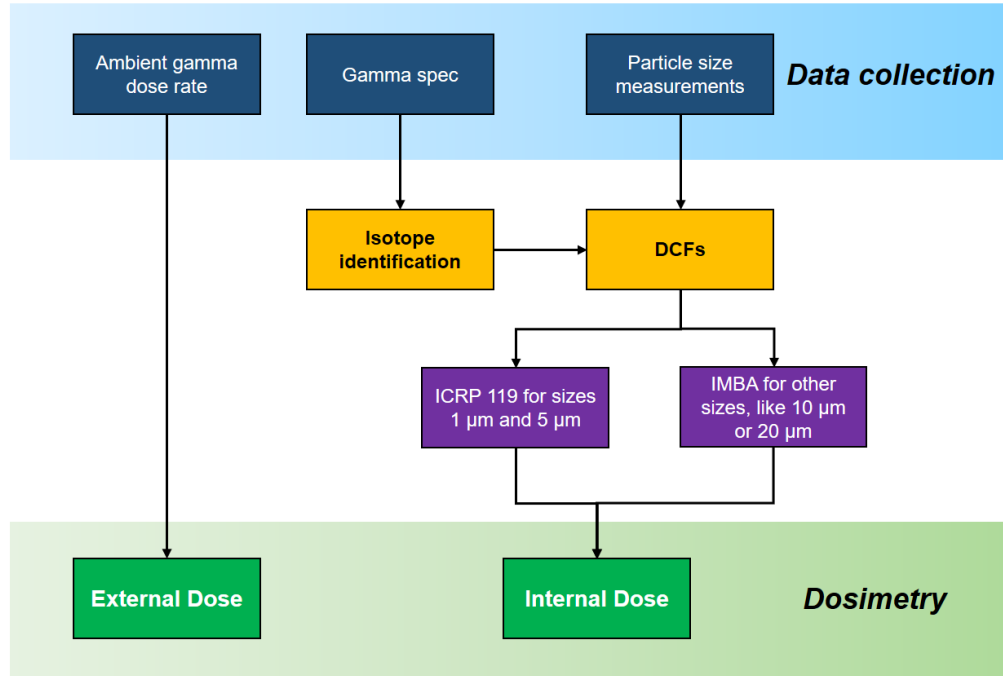


Figure 45: Summary of data to dosimetry process with the instrumentation used

As shown in the figure above, the dose rate obtained by the RadEye survey meter will allow for the external exposure to be determined, while the isotope identification data obtained from gamma spectroscopy using the URSA-II, in conjunction with the particle size distributions from the PA, will be able to provide estimates for internal dose. A sample calculation of a hypothetical scenario can be found in the Appendix.

4.4. Comparison of UGVs and UAVs

As mentioned in the introduction, unmanned aerial vehicles (UAVs) are also available in addition to ground vehicles (UGVs). While the use of UAVs is out of the scope of this work, it is important to briefly compare the two. Clearly, UAVs have the advantage of not being limited to pathways, views from greater latitude, and more degrees of control for the user. However, there are several benefits of UGVs. Specifically, UGVs such as the Husky

used in this project are more robust and can handle a heavier payload. As an example, the DJI Matrice UAV has a maximum payload of 15.5 kg and can only hover for a maximum of 18 minutes.¹⁰⁹

In the context of a nuclear accident, it would be difficult to attach the spectrometer, dose rate meter, air sampler, and a computer onto a UAV platform. UGVs also are superior for radiation measurement because they will, by definition, be closer to contamination on the ground surface, allowing for accurate, faster measurements. UAVs have difficulties associated with radiation measurement because they must hover at the exact same position in 3D.⁸³ Variations in altitude and position have found to yield inaccurate dose rate measurements.¹¹⁰ Additionally, the air sampling measurements obtained from a UAV would be inaccurate since the rotors used to fly the device influence the air currents in the UAV's surrounding area. UGVs also typically have longer battery lives compared to aerial vehicles.

4.5. Practical Considerations

There are several other factors to consider before deployment of the fully equipped Husky UGV into a high radiation, volatile environment. Neither the testing nor optimization performed in this work were done under harsh or realistic conditions. It is imperative to understand if the results would remain consistent when measuring a radioactive field or under complex air quality conditions (such as high winds, moisture, etc.). The impact of all of these devices on the battery life of the Husky UGV must also be

considered. The various components and their power consumption requirements are outlined in Table 15.

Table 15: Battery life of Husky UGV with added on detectors. The Husky’s battery lasts for 8 hours when on standby and 3 hours when moving. The total power available is 192V.

Device	Power Requirement	Internal Battery Life
RadEye Gamma Doserate Meter	2 AAA Batteries	900 hours
PurpleAir SD-II Air Quality sensor	Constant power required from UGV	N/A
URSA-II with NaI(Tl)	Constant power required from UGV (950 V)	N/A

To mitigate depleting battery life, an external generator can be placed on the detector’s platform to extend the battery life to many hours. Another important consideration for practical application is the mass of all of the added components onto the Husky UGV. The Husky’s all-terrain operating payload is 20.0 kg. The total mass of all supplementary detectors and components is outlined in Table 16. The combined mass of the components outlined in this work is approximately 8.24 kg; leaving 11.76 kg for other devices. These other devices can include LiDAR sensors and cameras.

Table 16: Total mass of additional components added to Husky UGV platform.

Device	Mass (kg)
RadEye Gamma Survey Meter	0.18
PurpleAir SD-II Air Quality Sensor	0.71
URSA-II	0.53
2×2 NaI(Tl)	0.90
MSI GT75 Titan	4.56
MSI Power Supply	1.36
Total	8.24
Husky UGV	50.0
Husky Maximum Payload	75.0
Husky All-Terrain Payload	20.0

4.6. Limitations

Over the course of these tests, there have been many technical difficulties with the various instrumentation. First and foremost, the URSA-II device was unable to recognize the NaI(Tl) scintillation detector connected to it, despite meeting the power and software requirements of the accompanying MCA software. The device was sent to the manufacturer for repair, but issues persisted with recognizing the detector. Paul Steinmeyer from

Radiation Safety Associates, Inc. graciously provided us with sample spectra for the two cases examined.

Next, the Husky UGV experienced consistent battery and power issues, which meant that tests with the current detector setup were unable to be performed. Additionally, the internal computer of the Husky UGV did not start up despite powering on the UGV itself, which meant that the controller could not connect and allow for the user to operate the robot. Discussions with Clearpath Robotics are currently ongoing to work to resolve these issues.

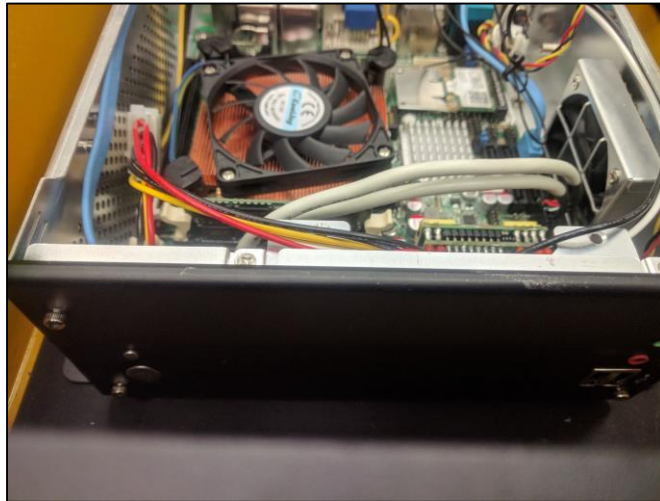


Figure 46: Malfunctioning internal computer of Husky UGV.

Since data was unable to be collected with the detectors using the Husky as a mode of transport, as a replacement, a dataset of gamma dose rate measurements was generated with the RadEye from simply walking in a set path, collecting the data for a scalar-integrated timeframe, and holding the detector at the same height as it would be if it were placed on top of the Husky UGV.

With regards to air sampling, prior to the use of the PurpleAir SD-II sensor, the GRIMM Portable Aerosol Spectrometer was tested extensively. While this device is able to provide more accurate experimental data with respect to particle sizing than the PA SD-II, it was unable to connect with the software on modern operating systems, as the GRIMM device was manufactured in the early 2000s and could only run on Windows XP. Additionally, the device was extremely sensitive to movement and was not designed for outdoor use, and would disconnect or shut off at the slightest disruption. As a result, it was determined that this device would not be suitable for implementation with the Husky UGV; if it were mounted onto the UGV it would neither connect to the natively developed software nor could it reliably demonstrate that it would remain running if the UGV were moving or if it had to move up and around an obstacle.



Figure 47: Close-up of the GRIMM Portable Aerosol Spectrometer.

Finally, the RadEye Bluetooth Low Energy (BLE) Adapter was a promising addition to the detector integration lineup, as it would be able to provide wireless communication of the RadEye readings to a user either through the accompanying mobile or desktop application. From here, a user would be able to record and download measurement history and logbook data. Unfortunately, the BLE adapter (seen in Figure 17)

attached to the RadEye used in our experiments was faulty, and was ultimately unable to transmit data to the desktop.

With all of these issues, a significant portion of time was devoted to understanding and attempting to fix the hardware and software issues, with a limited degree of success. Future work would therefore require that tests be carried out with each of these presently-malfunctioning devices in a fully operational state, or with adequate replacement devices.

Several different devices were explored in this study to determine the optimal combination of detectors that would provide a complete characterization of the radiation environment and allow for the mitigation requirements outlined in the regulatory SAMGs to be satisfied. Since the start of the project, the set of detectors has gone through several iterations as a result of technical difficulties, software incompatibilities, and general circumstances. Throughout the majority of this project, the COVID-19 pandemic was occurring which limited access to the laboratory. Despite these challenges, the experiments for this project were conducted.

5. Conclusions and Future Work

In this work, three detectors – the RadEye G Gamma Survey Meter, a NaI(Tl) scintillator paired with the URSA-II, and the PurpleAir SD-II Air Quality Sensor -were tested and optimized for use with the Husky UGV robotic platform. The optimal detector parameters comply with national and international severe accident management guidelines (SAMGs). Additionally, the Severe Accident Radioactivity Classification (SARC) MATLAB-based software was developed for the integration of detector data into a common interface, allowing for conservative external and internal dose estimations to be made following a severe accident scenario.

Future work involves further integration of the SARC software with the detectors. Ideally, the detector operation and results would be fully controllable using the software. Additionally, the MATLAB Bluetooth Communication function¹¹¹ will be utilized to seamlessly stream information from a (fully functioning) RadEye detector. As well, the operation of the URSA MCA software in ASCII mode must be assessed to determine if direct compatibility of the SARC with the URSA-II is feasible. If this is possible, the SARC software will have ultimately achieved its goal of allowing a user to comprehensively operate and analyze the incoming data from the three detectors in one location.

Furthermore, the SARC software would also be programmed to provide basic dosimetric estimates, for both internal and external exposures, allowing emergency personnel to easily and quickly triage exposed individuals. The accuracy of these results can be improved through the use of more robust data. For example, the dose conversion factors outlined in ICRP 119 (seen in Table A.1 in the Appendix) can be determined for

particle sizes other than 1 and 5 μm using the IMBA software. This increased customizability would allow the SARC software to provide results for the user with more accuracy.

Future studies can also look to quantify the radiation hardness of each device and its components. Specifically, the use of the PA sensor for robotic radiation monitoring in a severe nuclear accident setting has not been studied prior to this work, and so the radiation tolerance of the PA must also be assessed with the relevant radiological conditions. As previously mentioned, this work evaluated each component in ideal, stable conditions. For practical use, their function and robustness in a harsh, realistic environment must also be validated.

Finally, the ideal next evolution of the robot for the post nuclear accident scenario would be its use for assessing structural damage to buildings using its cameras in conjunction with computer vision. In a real-life scenario, if the robot is already collecting data outside the perimeter of the facility, it would make sense to, on the same deployment, record and assess any potential damage to reactor or vacuum buildings, at least at the ground level. This can be done using computer vision algorithms to detect cracks in concrete, as well as the depth of said cracks using infrared and video cameras.

References

1. Pioneer Helps With Chernobyl Clean-Up. Robot Mag.
<http://www.botmag.com/pioneer-helps-chernobyl-clean/>. Published 2006.
Accessed July 10, 2021.
2. Kawatsuma S, Fukushima M, Okada T. Emergency response by robots to Fukushima-Daiichi accident: summary and lessons learned. *Ind Robot An Int J*. 2012;39(5):428-435. doi:10.1108/01439911211249715
3. Purple Air. PurpleAir PA-II-SD Air Quality Detector | PM2.5 Measurement Device. <https://www2.purpleair.com/products/purpleair-pa-ii-sd>. Accessed July 11, 2021.
4. World Nuclear Association. Safety of Nuclear Reactors. <https://www.world-nuclear.org/information-library/safety-and-security/safety-of-plants/safety-of-nuclear-power-reactors.aspx>. Published 2021. Accessed July 9, 2021.
5. Bureau of Aircraft Accidents Archives. Accidents statistics. <http://www.baaa-acro.com/crashes-statistics>. Accessed July 9, 2021.
6. World Health Organization. The human consequences of the Chernobyl nuclear accident: A strategy for recovery. <https://www.who.int/publications/m/item/the-human-consequences-of-the-chernobyl-nuclear-accident-a-strategy-for-recovery>. Published 2002. Accessed July 9, 2021.
7. Barquinero JF, Fattibene P, Chumak V, et al. Lessons from past radiation accidents: Critical review of methods addressed to individual dose assessment of

- potentially exposed people and integration with medical assessment. *Environ Int.* 2021;146:106175. doi:10.1016/J.ENVINT.2020.106175
8. International Atomic Energy Agency. *Defence in Depth in Nuclear Safety.*; 1996. <https://www.iaea.org/publications/4716/defence-in-depth-in-nuclear-safety>. Accessed July 9, 2021.
 9. Canadian Nuclear Safety Commission (CNSC-CCSN). *REGDOC-2.4.1, Deterministic Safety Analysis.*; 2014. <https://nuclearsafety.gc.ca/eng/acts-and-regulations/regulatory-documents/published/html/regdoc2-4-1/index.cfm>. Accessed July 9, 2021.
 10. Canadian Nuclear Safety Commission (CNSC-CCSN). E-DOCS#3841774 - Guidance on Safety Analysis for Nuclear Powere Plants GD-310. 2012.
 11. Canadian Nuclear Safety Commission (CNSC-CCSN). *REGDOC-2.5.2, Design of Reactor Facilities: Nuclear Power Plants.*; 2014. <https://nuclearsafety.gc.ca/eng/acts-and-regulations/regulatory-documents/published/html/regdoc2-5-2/index.cfm>. Accessed July 10, 2021.
 12. International Atomic Energy Agency (IAEA). *INES: The International Nuclear and Radiological Event Scale User's Manual.*; 2009. <https://www.iaea.org/publications/10508/ines-the-international-nuclear-and-radiological-event-scale-users-manual>. Accessed July 16, 2021.
 13. Tuttle RM, Becker D V. The Chernobyl accident and its consequences: Update at the millennium. *Semin Nucl Med.* 2000;30(2):133-140. doi:10.1053/NM.2000.5412

14. Aitsi-Selmi A, Murray V. The Chernobyl Disaster and Beyond: Implications of the Sendai Framework for Disaster Risk Reduction 2015–2030. *PLoS Med.* 2016;13(4). doi:10.1371/JOURNAL.PMED.1002017
15. Mullner N. Three Decades after Chernobyl: Technical or Human Causes? 2019;323-340. doi:10.1007/978-3-658-25987-7_15
16. Zablotska LB. 30 years After the Chernobyl Nuclear Accident: Time for Reflection and Re-evaluation of Current Disaster Preparedness Plans. *J Urban Health.* 2016;93(3):407. doi:10.1007/S11524-016-0053-X
17. The International Chernobyl Project. *Surface Contamination Map.* https://www-pub.iaea.org/MTCD/publications/PDF/Pub886_web/Chernobylmap1.html. Accessed July 10, 2021.
18. Gauntt R, Kalinich D, Cardoni J, et al. SANDIA REPORT Fukushima Daiichi Accident Study (Status as of April 2012). <http://www.ntis.gov/help/ordermethods.asp?loc=7-4-0#online>. Accessed July 10, 2021.
19. Nagatani K, Kiribayashi S, Okada Y, et al. Emergency response to the nuclear accident at the Fukushima Daiichi Nuclear Power Plants using mobile rescue robots. *J F Robot.* 2013;30(1):44-63. doi:10.1002/ROB.21439
20. Anzai K, Ban N, Ozawa T, Tokonami S. Fukushima Daiichi Nuclear Power Plant accident: facts, environmental contamination, possible biological effects, and countermeasures. *J Clin Biochem Nutr.* 2012;50(1):2. doi:10.3164/JCBN.D-11-00021

21. Kai M, Homma T, Lochard J, et al. *ICRP Publication 146: Radiological Protection of People and Environment in the Event of a Large Nuclear Accident*. [https://icrp.org/publication.asp?id=ICRP Publication 146](https://icrp.org/publication.asp?id=ICRP%20Publication%20146). Accessed July 10, 2021.
22. Kraft G, Krämer M. Linear Energy Transfer and Track Structure. *Adv Radiat Biol*. 1993;17:1-52. doi:10.1016/B978-0-12-035417-7.50004-0
23. ICRU Report 16. *J Int Comm Radiat Units Meas*. 1970;os9(1):NP-NP. doi:10.1093/JICRU/OS9.1.REPORT16
24. Schuff JA, Policastro L, Durán H, et al. Relative biological effectiveness measurements of low energy proton and lithium beams on tumor cells. *Nucl Instruments Methods Phys Res Sect B Beam Interact with Mater Atoms*. 2002;187(3):345-353. doi:10.1016/S0168-583X(01)01136-3
25. Conte V, Selva A, Colautti P, Hilgers G, Rabus H. Track structure characterization and its link to radiobiology. *Radiat Meas*. 2017;106:506-511.
26. Podgorsak ED, International Atomic Energy Agency. *Radiation Oncology Physics : A Handbook for Teachers and Students*. International Atomic Energy Agency; 2005. https://inis.iaea.org/search/search.aspx?orig_q=RN:36071456. Accessed July 2, 2019.
27. Valentin J, Cox R, Kellerer AM. Relative biological effectiveness (RBE), quality factor (Q), and radiation weighting factor (wR). *Ann ICRP*. 2003;33(4):1-121. doi:10.1016/S0146-6453(03)00024-1
28. Hall EJ, Giaccia AJ. *Radiobiology for the Radiologist*.

29. International Commission on Radiological Protection (ICRP). *ICRP Publication 103: The 2007 Recommendations of the International Commission on Radiological Protection.*; 2007. doi:10.1177/ANIB_37_2-4
30. International Atomic Energy Agency (IAEA). *Safety of Nuclear Power Plants: Commissioning and Operation.*; 2016.
<https://www.iaea.org/publications/10886/safety-of-nuclear-power-plants-commissioning-and-operation>. Accessed July 10, 2021.
31. Canadian Nuclear Safety Commission (CNSC-CCSN). *REGDOC-2.10.1: Nuclear Emergency Preparedness and Response.*; 2014.
<https://nuclearsafety.gc.ca/eng/acts-and-regulations/regulatory-documents/published/html/regdoc2-10-1/index.cfm#sec1>. Accessed July 10, 2021.
32. International Atomic Energy Agency (IAEA). Accident Management Programmes for Nuclear Power Plants. <https://www.iaea.org/publications/12378/accident-management-programmes-for-nuclear-power-plants>. Published 2019. Accessed July 10, 2021.
33. Ohno K, Kawatsuma S, Okada T, Takeuchi E, Higashi K, Tadokoro S. Robotic control vehicle for measuring radiation in Fukushima Daiichi Nuclear Power Plant. In: *9th IEEE International Symposium on Safety, Security, and Rescue Robotics, SSRR 2011.* ; 2011:38-43. doi:10.1109/SSRR.2011.6106792
34. Canadian Nuclear Safety Commission (CNSC-CCSN). *REGDOC-2.3.2: Accident Management, Version 2.*; 2015. <https://nuclearsafety.gc.ca/eng/acts-and-regulations/regulatory-documents/published/html/regdoc2-3-2v2/index.cfm>.

Accessed July 10, 2021.

35. Tsujiguchi T, Suzuki Y, Sakamoto M, et al. Simulation study on radiation exposure of emergency medical responders from radioactively contaminated patients. *Sci Rep.* 2021;11(1):6162. doi:10.1038/S41598-021-85635-2
36. Orita M, Hayashida N, Taira Y, et al. Measurement of individual doses of radiation by personal dosimeter is important for the return of residents from evacuation order areas after nuclear disaster. *PLoS One.* 2015;10(3). doi:10.1371/JOURNAL.PONE.0121990
37. International Atomic Energy Agency. Personnel Radiation Dosimetry. *Proc a Tech Comm Meet to Elabor Proced Data Intercomp Pers Dosimeters Organ by IAEA.* 1985.
38. Canadian Nuclear Safety Commission (CNSC-CCSN). Introduction to Dosimetry, INFO-0827. 2012.
39. Kry SF, Alvarez P, Cygler JE, et al. AAPM TG 191: Clinical use of luminescent dosimeters: TLDs and OSLDs. *Med Phys.* 2020;47(2):e19-e51. doi:10.1002/MP.13839
40. Bailiff IK, Sholom S, McKeever SWS. Retrospective and emergency dosimetry in response to radiological incidents and nuclear mass-casualty events: A review. *Radiat Meas.* 2016;94:83-139. doi:10.1016/J.RADMEAS.2016.09.004
41. Bøtter-Jensen L, McKeever SWS, Wintle AG. Passive optically stimulated luminescence dosimetry. *Opt Stimul Lumin Dosim.* January 2003:101-118.

doi:10.1016/B978-044450684-9/50091-X

42. Grishkov AA, Korolev YD, Shklyayev VA. Monte Carlo simulation for development of electron avalanches in nitrogen at moderate and high reduced electric field. *Phys Plasmas*. 2020;27(10):103504. doi:10.1063/5.0021194
43. Brunner G. Townsend coefficients of gases in avalanche counters. *Nucl Instruments Methods*. 1978;154(1):159-163. doi:10.1016/0029-554X(78)90673-0
44. Takata N, Matsumoto T. The effect of the applied voltage on ionization in a parallel plate ionization chamber. *Nucl Instruments Methods Phys Res Sect A Accel Spectrometers, Detect Assoc Equip*. 1991;302(2):327-330. doi:10.1016/0168-9002(91)90416-N
45. Almutairi B, Alam S, Akyurek T, Goodwin CS, Usman S. Experimental evaluation of the deadtime phenomenon for GM detector: deadtime dependence on operating voltages. *Sci Reports 2020 101*. 2020;10(1):1-15. doi:10.1038/s41598-020-75310-3
46. Knoll G. *Radiation Detection and Measurement*. 3rd ed. New York: Wiley; 1989. <https://catalogue.nla.gov.au/Record/179294>. Accessed July 7, 2021.
47. Thermo Fischer Scientific. RO-20 Ion Chamber Survey Meters. <https://www.thermofisher.com/order/catalog/product/RO20#/RO20>. Accessed July 7, 2021.
48. Parrott-Sheffer C. Instrumentation - Proportional Counters. In: *Encyclopaedia Britannica*. ; 1998. <https://www.britannica.com/technology/proportional-counter>.

Accessed July 7, 2021.

49. Ludlum Inc. Model 26-1 Integrated Frisker. <https://ludlums.com/products/all-products/product/model-26-1>. Accessed July 7, 2021.
50. Moser SW, Harder WF, Hurlbut CR, Kusner MR. Principles and practice of plastic scintillator design. *Radiat Phys Chem.* 1993;41(1-2):31-36. doi:10.1016/0969-806X(93)90039-W
51. Kim D geon, Lee S, Park J, et al. Performance of 3D printed plastic scintillators for gamma-ray detection. *Nucl Eng Technol.* 2020;52(12):2910-2917.
52. Lecoq P, Gektin A, Korzhik M. *Inorganic Scintillators for Detector Systems.* 2017. doi:10.1007/978-3-319-45522-8
53. Bizarri G. Scintillation mechanisms of inorganic materials: From crystal characteristics to scintillation properties. *J Cryst Growth.* 2010;312(8):1213-1215. doi:10.1016/J.JCRYSGRO.2009.12.063
54. Novotny R. Inorganic scintillators—a basic material for instrumentation in physics. *Nucl Instruments Methods Phys Res Sect A Accel Spectrometers, Detect Assoc Equip.* 2005;537(1-2):1-5. doi:10.1016/J.NIMA.2004.07.221
55. Derenzo SE, Weber MJ, Bourret-Courchesne E, Klintonberg MK. The quest for the ideal inorganic scintillator. *Nucl Instruments Methods Phys Res Sect A Accel Spectrometers, Detect Assoc Equip.* 2003;505(1-2):111-117. doi:10.1016/S0168-9002(03)01031-3
56. Mao R, Zhang L, Zhu RY. Optical and scintillation properties of inorganic

- scintillators in high energy physics. *IEEE Trans Nucl Sci.* 2008;55(4):2425-2431.
doi:10.1109/TNS.2008.2000776
57. Hamamatsu. *Photomultiplier Tubes: Basics and Applications*. 3A ed. Hamamatsu, Japan; 2007.
 58. Polyakov S V. Photomultiplier tubes. 2013. doi:10.1016/B978-0-12-387695-9.00003-2
 59. SENSE. Photomultiplier Tubes (PMT). <https://www.sense-pro.org/ill-sensors/pmt>. Accessed July 8, 2021.
 60. Canadian Nuclear Safety Commission. Study of Consequences of a Hypothetical Severe Nuclear Accident and Effectiveness of Mitigation Measures. 2015.
 61. Rojavin Y, Seamon MJ, Tripathi RS, et al. Civilian nuclear incidents: An overview of historical, medical, and scientific aspects. *J Emergencies, Trauma Shock.* 2011;4(2):260. doi:10.4103/0974-2700.82219
 62. Lavelle KB, Essex RM, Carney KP, Cessna JT, Hexel CR. A reference material for evaluation of ¹³⁷Cs radiochronometric measurements. *J Radioanal Nucl Chem.* 2018;318(1):195-208. doi:10.1007/S10967-018-6061-4
 63. “File:Cs-137-decay.svg” - Wikimedia Commons.
<https://commons.wikimedia.org/wiki/File:Cs-137-decay.svg>. Accessed July 8, 2021.
 64. File:Cobalt-60 Decay Scheme.svg - Wikimedia Commons.
https://commons.wikimedia.org/wiki/File:Cobalt-60_Decay_Scheme.svg.

Accessed July 8, 2021.

65. Armstrong BK, Woodliff HJ. Studies on the ^{57}Co vitamin B12 plasma level absorption test. *J Clin Pathol*. 1970;23(7):569. doi:10.1136/JCP.23.7.569
66. Cember H, Johnson T. *Introduction to Health Physics*. McGraw-Hill Medical; 2009.
https://books.google.com/books/about/Introduction_to_Health_Physics_Fourth_Ed.html?id=8BhgmAEACAAJ. Accessed July 8, 2021.
67. Tsitsimpelis I, Taylor CJ, Lennox B, Joyce MJ. A review of ground-based robotic systems for the characterization of nuclear environments. *Prog Nucl Energy*. 2019;111:109-124. doi:10.1016/J.PNUCENE.2018.10.023
68. Moore T. Robots for nuclear power plants. *IAEA Bull*. 1985.
69. International Atomic Energy Agency (IAEA). *State of the Art Technology for Decontamination and Dismantling of Nuclear Facilities.*; 1999.
<https://www.iaea.org/publications/5783/state-of-the-art-technology-for-decontamination-and-dismantling-of-nuclear-facilities>. Accessed July 10, 2021.
70. Lam Loong Man CKY, Koonjul Y, Nagowah L. A low cost autonomous unmanned ground vehicle. *Futur Comput Informatics J*. 2018;3(2):304-320. doi:10.1016/J.FCIJ.2018.10.001
71. Lobo N. University of Texas “Opens Doors” to Safer Nuclear Waste Retrieval. Clearpath Robotics. <https://clearpathrobotics.com/blog/2018/08/university-texas-opens-doors-safer-nuclear-waste-retrieval/>. Published 2018. Accessed July 10,

- 2021.
72. New robot dog Spot turning heads at OPG. Ontario Power Generation.
<https://www.opg.com/stories/new-robot-dog-spot-turning-heads-at-opg/>. Published 2021. Accessed July 10, 2021.
 73. Frankenberg F von, McDougall R, Nokleby S, Waller E. A Mobile Robotic Platform for Generating Radiation Maps. *Lect Notes Comput Sci (including Subser Lect Notes Artif Intell Lect Notes Bioinformatics)*. 2012;7507 LNAI(PART 2):407-416. doi:10.1007/978-3-642-33515-0_41
 74. McDougall R, Nokleby SB, Waller E. Probabilistic-Based Robotic Radiation Mapping Using Sparse Data. *J Nucl Eng Radiat Sci*. 2018;4(2). doi:10.1115/1.4038185
 75. Miller A, Machrafi R, Mohany A. Development of a semi-autonomous directional and spectroscopic radiation detection mobile platform. *Radiat Meas*. 2015;72:53-59. doi:10.1016/J.RADMEAS.2014.11.009
 76. Hosmar ME. Development of an autonomous radiation mapping robot. April 2017. <http://ir.library.dc-uoit.ca/handle/10155/791>. Accessed July 10, 2021.
 77. Clearpath. Jackal UGV - Small Weatherproof Robot.
<https://clearpathrobotics.com/jackal-small-unmanned-ground-vehicle/>. Accessed July 10, 2021.
 78. Andersonl RB, Pryor M, Landsberger S. Mobile robotic radiation surveying using recursive Bayesian estimation. *IEEE Int Conf Autom Sci Eng*. 2019;2019-

August:1187-1192. doi:10.1109/COASE.2019.8843064

79. Anderson RB, Pryor M, Abeyta A, Landsberger S. Mobile Robotic Radiation Surveying With Recursive Bayesian Estimation and Attenuation Modeling. *IEEE Trans Autom Sci Eng.* 2020. doi:10.1109/TASE.2020.3036808
80. Kazemeini M, Barzilov A, Lee J, Yim W. Integration of CZT and CLYC radiation detectors into robotic platforms using ROS. *AIP Conf Proc.* 2019;2160(1):050019. doi:10.1063/1.5127711
81. A S, J H, D S, et al. The use of a CZT detector with robotic systems. *Appl Radiat Isot.* 2020;166. doi:10.1016/J.APRADISO.2020.109395
82. Vetter K, Barnowski R, Cates JW, et al. Advances in Nuclear Radiation Sensing: Enabling 3-D Gamma-Ray Vision. *Sensors (Basel).* 2019;19(11). doi:10.3390/S19112541
83. Gabrlik P, Lazna T, Jilek T, Sladek P, Zalud L. An automated heterogeneous robotic system for radiation surveys: Design and field testing. *J F Robot.* 2021;38(5):657-683. doi:10.1002/ROB.22010
84. Ghawaly JM, Nicholson AD, Peplow DE, et al. Data for training and testing radiation detection algorithms in an urban environment. *Sci Data* 2020 71. 2020;7(1):1-6. doi:10.1038/s41597-020-00672-2
85. Han J, Xu Y, Di L, Chen Y. Low-cost Multi-UAV Technologies for Contour Mapping of Nuclear Radiation Field. *J Intell Robot Syst* 2012 701. 2012;70(1):401-410. doi:10.1007/S10846-012-9722-5

86. Šálek O, Matolín M, Gryc L. Mapping of radiation anomalies using UAV mini-airborne gamma-ray spectrometry. *J Environ Radioact*. 2018;182:101-107. doi:10.1016/J.JENVRAD.2017.11.033
87. Redwan Newaz A Al, Jeong S, Lee H, Ryu H, Chong NY. UAV-based multiple source localization and contour mapping of radiation fields. *Rob Auton Syst*. 2016;85:12-25. doi:10.1016/J.ROBOT.2016.08.002
88. Cai C, Carter B, Srivastava M, Tsung J, Vahedi-Faridi J, Wiley C. Designing a radiation sensing UAV system. *2016 IEEE Syst Inf Eng Des Symp SIEDS 2016*. June 2016:165-169. doi:10.1109/SIEDS.2016.7489292
89. International Commission on Radiation Units and Measurements (ICRU). ICRU Report 92, Radiation Monitoring for Protection of the Public after Major Releases of Radionuclides to the Environment. <https://www.icru.org/report/icru-report-92-radiation-monitoring-for-protection-of-the-public-after-major-releases-of-radionuclides-to-the-environment-2/>. Accessed July 16, 2021.
90. Clearpath. Husky UGV - Outdoor Field Research Robot by Clearpath. <https://clearpathrobotics.com/husky-unmanned-ground-vehicle-robot/>. Accessed July 11, 2021.
91. ThermoFisher Scientific. RadEye™ G Series Personal Dose Rate Meters. <https://www.thermofisher.com/order/catalog/product/4250674#/4250674>. Accessed July 11, 2021.
92. NIST - SRM Order Request System SRM 1649b - Urban Dust. https://www-s.nist.gov/srmors/view_detail.cfm?srm=1649B. Accessed July 11, 2021.

93. NIST - SRM Order Request System SRM 2583 - Trace Elements in Indoor Dust (Nominal Mass Fraction of 90 mg/kg Lead)
. https://www-s.nist.gov/srmors/view_detail.cfm?srm=2583. Accessed July 11, 2021.
94. CR G, BR F, DJ F-K, P H. Description of Particle Size, Distribution, and Behavior of Talc Preparations Commercially Available Within the United States. *J Bronchology Interv Pulmonol*. 2018;25(1):25-30.
doi:10.1097/LBR.0000000000000420
95. Python Programming Language. <https://www.python.org/>. Accessed July 11, 2021.
96. TkInter - Python Wiki. <https://wiki.python.org/moin/TkInter>. Accessed July 11, 2021.
97. Overview — NumPy v1.21 Manual. <https://numpy.org/doc/stable/>. Accessed July 11, 2021.
98. SciPy.org — SciPy.org. <https://www.scipy.org/>. Accessed July 11, 2021.
99. MATLAB - MathWorks - MATLAB & Simulink.
<https://www.mathworks.com/products/matlab.html>. Accessed July 11, 2021.
100. Canadian Nuclear Safety Commission (CNSC-CCSN). Natural Background Radiation in Canada. <http://nuclearsafety.gc.ca/eng/resources/maps-of-nuclear-facilities/background-radiation.cfm#instructions>. Published 2014. Accessed July 10, 2021.
101. Deslattes R, Kessler E, Indelicato P, et al. X-Ray Transition Energies Database. NIST, Physical Laboratory. <https://www.nist.gov/pml/x-ray-transition-energies->

- database. Published 2005. Accessed July 10, 2021.
102. Eckerman K, Harrison J, Menzel H, Clement C. *Compendium of Dose Coefficients Based on ICRP Publication 60*. <https://www.icrp.org/publication.asp?id=ICRP> Publication 119. Accessed July 11, 2021.
 103. International Atomic Energy Agency (IAEA). *Assessment of Equipment Capability to Perform Reliably under Severe Accident Conditions (TECDOC 1818)*.; 2017. <https://www.iaea.org/publications/12218/assessment-of-equipment-capability-to-perform-reliably-under-severe-accident-conditions>. Accessed July 11, 2021.
 104. Musolino S. Evaluation of Preventative Radiological/Nuclear Detector Archetypes to Validate Repurpose to the Consequence Management Mission. September 2017. doi:10.2172/1425190
 105. National Council on Radiation Protection and Measurements. *Responding to a Radiological or Nuclear Terrorism Incident: A Guide for Decision Makers*.
 106. International Atomic Energy Agency (IAEA). *Basic Principles Objectives IAEA Nuclear Energy Series Accident Monitoring Systems for Nuclear Power Plants Accident Monitoring Systems for Nuclear Power Plants*.; 2015. <http://www.iaea.org/Publications/index.html>. Accessed July 11, 2021.
 107. Public Health England. IMBA® Internal Dosimetry Software. <https://www.phe-protectionservices.org.uk/imba>. Accessed July 16, 2021.
 108. Garland J. The Essential CANDU - A Textbook on the CANDU Nuclear Power Plant Technology. 2014:1530.

109. DJI. Matrice 600 Pro - Product Information. <https://www.dji.com/ca/matrice600-pro/info#specs>. Accessed July 11, 2021.
110. Gabrlik P, Lazna T. Simulation of Gamma Radiation Mapping Using an Unmanned Aerial System. *IFAC-PapersOnLine*. 2018;51(6):256-262. doi:10.1016/J.IFACOL.2018.07.163
111. Bluetooth Communication - MATLAB & Simulink. <https://www.mathworks.com/help/instrument/bluetooth-communication.html>. Accessed July 11, 2021.
112. World Health Organization. *Preliminary dose estimation from the nuclear accident after the 2011 Great East Japan Earthquake and Tsunami*. WHO Press, 2012. <https://www.who.int/publications/i/item/9789241503662>. Accessed July 11, 2021.

Appendix

Table A.1: Radionuclides posing internal radiation hazards at CANDU facilities

Radionuclide		T _{1/2}	Type	f ₁	Inhalation DCF (from ICRP119 Table A.1*), e (Sv/Bq)	
					1 um	5 um
Fission Products	Cs-137	30.0 y	F	1.0	4.8E-09	6.7E-09
	I-131	8.04 d	F	1.0	7.6E-09	1.1E-08
	Sr-90	29.12 y	F	0.3	2.4E-08	3.0E-08
			S	0.01	1.5E-07	7.7E-08
	Y-90	64.0 h	M	0.0001	1.4E-09	1.6E-09
			S	0.0001	1.5E-09	1.7E-09
	Ce-141	32.501 d	M	0.0005	3.1E-09	2.7E-09
			S	0.0005	3.6E-09	3.1E-09
System Activation Products	Co-60	5.271 y	M	0.1	9.6E-09	7.1E-09
			S	0.05	2.9E-08	1.7E-08
	Fe-59	44.529 d	F	0.1	2.2E-09	3.0E-09
			M	0.1	3.5E-09	3.2E-09
	Mn-54	312.5 d	F	0.1	8.7E-10	1.1E-09
			M	0.1	1.5E-09	1.2E-09
Fuel Activation Products	Pu-239	24065 y	M	0.0005	4.7E-05	3.2E-05
			S	0.00001	1.5E-05	8.3E-06
	Am-241	432.2 y	M	0.0005	3.9E-05	2.7E-05

*Table A.1 in ICRP 119, 'Effective dose coefficients (e) for ingested and inhaled particulates (activity median aerodynamic diameters (AMAD) of 1 and 5 um) for workers'.

For the inhalation dose coefficients outlined¹⁰², the particulates are also organized by material type. Type V, F, M, and S refer to deposited materials that are absorbed into

the blood from the respiratory tract with a very fast, fast, moderate, and slow rate of absorption, respectively; the range of fission products, system activation products, and fuel activation products that are classified as CANDU radiological releases are covered here.¹⁰⁸

SARC Internal Dose Assessment: Hypothetical CANDU Accident Scenario

The air particles sampled in this study were taken approximately 8 kilometres away from the Pickering Nuclear Generating Station (NGS), seen in Figure A.1.



Figure A.1: Satellite view of Pickering Nuclear Generating Station.

If these samples represented accident conditions at the Pickering NGS resulting from a plume passing by, it is important to determine the internal dose resulting from

inhalation. This can be determined in the SARC software using the method outlined in ICRP 119, seen in equation (4).

$$Intake [Bq] = BR \left[\frac{m^3}{hr} \right] \cdot C_{air} \left[\frac{particles}{m^3} \right] \cdot t[hr] \quad (4)$$

The inhalation intake is given as the product of the breathing rate (defined as 1.2 cubic metres per hour in ICRP 119), the concentration of air (in particles per hour, assumed here to be a given value from the PA sensor for 1 or 5 μm during the dust sensitivity tests), and the exposure time (in hours; assumed to be 0.17 h, since the PA data used is for 10-minute average sampling time). The intake is then used to determine the committed effective dose (CED, in Sv), seen in equation (5),

$$CED [Sv] = Intake [Bq] \cdot DCF \left[\frac{Sv}{Bq} \right] \quad (5)$$

which is the product of the intake and the inhalation dose conversion factors outlined in ICRP 119 for a given radionuclide of sizes 1 and 5 μm (Table A.1). The major, conservative assumption made here is that the air particles sampled are *all* radioactive, since the PA cannot differentiate whether particles are radioactive or not. As outlined in regulatory documentation^{32, 103}, conservative estimates are preferred for severe accident analysis.

As mentioned above, the concentration values were determined for 1 and 5 μm from the dust sensitivity tests with the PA, since radioactive material attaches to dust; as such the values are set to 9.2 particles per dl (92,000 particles per cubic metre) and 0.07 particles per dl (700 particles per cubic metre) for 1 and 5 μm , respectively.

With these assumptions, the internal dose resulting from inhalation of Co-60, Cs-137, and I-131 (assumed CANDU releases) was determined in the SARC software, and is outlined in Table A.2 below in mSv.

Table A.2: Internal dose resulting from inhalation in hypothetical accident scenario for various CANDU release products.

CANDU Releases	Inhalation dose (mSv)	
	1 μm	5 μm
Co-60	0.1802	0.0010
Cs-137	0.0901	0.0010
I-131	0.1426	0.0016

The results determined are in the correct order of magnitude for a severe accident and for the assumed sampling time of the airborne particles. The values are also consistent with internal dose estimations made from Chernobyl and Fukushima resulting from inhalation for individuals located in the range of 5 to 15 km away from the accident site ^{6,112}. In this sense, the assumptions are again considered to be conservative, since the internal dose values are comparable to those attributed to Chernobyl and Fukushima-type accidents, which cannot or are extremely unlikely to occur in Canada ⁶⁰.